RSC Advances

PAPER

View Article Online
View Journal | View Issue

Cite this: *RSC Adv.*, 2026, **16**, 10984

Waste-derived mesoporous biochar for glycerol to glycerol carbonate upgrading: intensified process design and techno-economic analysis

Phonsan Saetiao, Napaphat Kongrit and Jakkrapong Jitjamnong *

Biochar-based green catalysts are increasingly important for sustainable chemical manufacturing, offering a low-cost and environmentally friendly approach to catalysts by utilizing agricultural waste materials rich in natural minerals. This study developed a self-activated potassium-rich mesoporous biochar catalyst derived from banana bunch stalks (BS) for glycerol carbonate (GyC) synthesis *via* transesterification with dimethyl carbonate (DMC). Unlike conventional alkali-impregnated catalysts, the biochar exhibited intrinsic basic active sites without any external chemical modification, enhancing its sustainability and cost-effectiveness. BS, an abundant agricultural waste material with a high alkaline content, were transformed into a heterogeneous catalyst through controlled pyrolysis. The research employed response surface methodology with a central composite design to optimize the reaction conditions for GyC yield. The highest GyC yield was found to be 92.40%, under the derived optimal conditions of: 3.45 wt% catalyst loading, 3.58 : 1 DMC : glycerol molar ratio, 90 °C reaction temperature, and 119 min reaction time. Detailed characterization showed that the catalyst's high potassium content and strong basicity (3.66 mmol g^{-1}) contributed to its catalytic efficiency, establishing a clear structure–activity relationship between intrinsic mineral species and performance. Kinetic studies revealed that the reaction follows a pseudo-first-order mechanism with an activation energy of 55.70 kJ mol^{-1}, confirming a chemically controlled regime under optimized conditions. Importantly, this study integrates catalyst development, reaction optimization, kinetic modelling, process simulation, and techno-economic evaluation within a unified framework, providing a comprehensive assessment of industrial feasibility. Process simulation validated the scalability of the optimized process, achieving a product enrichment of near purity (99.9%). Techno-economic analysis demonstrated that larger production capacities significantly enhanced the profitability, reducing the payback period, and increasing the net present value and internal rate of return. This work demonstrates a scalable waste-to-value catalytic platform that advances circular bioeconomy strategies and sustainable chemical manufacturing for high-value glycerol upgrading.

Received 7th December 2025
Accepted 18th February 2026

DOI: 10.1039/d5ra09460g

rsc.li/rsc-advances

1. Introduction

The move toward sustainable energy around the world has increased the use of biodiesel as a renewable replacement for fossil fuels. Biodiesel is known for its lower greenhouse gas emissions and biodegradability, making it an important component in climate change mitigation strategies.[1] However, biodiesel production also generates a significant by-product: crude glycerol (CG). This material makes up about 10% of all biodiesels produced by weight, causing a surplus that lowers its market value and complicates disposal.[2,3] By 2027, the global amount of CG produced is projected to reach almost 3.9 billion liters per year due to continued expansion of the biodiesel industry.[4] Therefore, innovative strategies are urgently needed to increase the worth of CG, changing it from a low-value secondary material into significant value-added chemicals, which can improve the economics and environmental stability of biodiesel production.[1–3]

Among the possible materials made from glycerol is glycerol carbonate (GyC), which has become particularly promising because of its flexible use in industries. For example, GyC is a significant chemical used in medicines, polymers, cosmetics, and electronics. As a biodegradable solvent, an element in organic synthesis, and part of environmentally safe materials like biodegradable plastics and coatings, the demand for GyC has increased in the global markets.[4] The creation of GyC addresses the surplus of CG and also follows circular bio-economy ideas by changing waste into useful items.

Several methods for the synthesis of GyC exist, including direct carbonation with carbon dioxide (CO_2),[5–7] urea-based synthesis,[8,9] and transesterification with organic

Petroleum Technology Program, Faculty of Industrial Education and Technology, Rajamangala University of Technology Srivijaya, 2/1 Rachadamnoennork Rd., Boryang, Muang, Songkhla 90000, Thailand. E-mail: jakkrapong.j@rmutsv.ac.th; Fax: +66 7 4317178; Tel: +66 85 921 9559

carbonates.[10–13] Of these pathways, transesterification with dimethyl carbonate (DMC) has gained attention because of its effectiveness and environmental friendliness.[1,14,15] The use of DMC is preferred because of its low toxicity, ability to break down naturally, and significant reactivity. These features make it a good substitute for normal carbonylation agents, which often use dangerous secondary materials and lead to environmental worries.[16] Through a sustainable method, the transesterification reaction between glycerol and DMC provides GyC under mild reaction conditions with minimal environmental harm.

Catalysis plays a critical part in improving the transesterification process. To assist this reaction, homogeneous and heterogeneous catalysts have been used. Although homogeneous catalysts, such as alkali metal hydroxides or alkoxides, often achieve high conversion rates, it is difficult to recover the catalyst, separate it from the reaction mixture and provide environmental safety. These limitations have increased interest in heterogeneous catalysts, as they can be recycled, are stable under reaction conditions, and can be separated from reaction products easily. Heterogeneous catalysts are attractive for industrial applications because they can lower operational expenses and reduce the environmental footprints.[17–19]

In recent years catalysts based on biochar have become a sustainable option to traditional heterogeneous catalysts. Biochar is a carbon-rich substance made from biomass pyrolysis under limited oxygen. It has a notable surface area, porosity, and changeable chemical properties, which make it an excellent choice for catalytic uses. Using biochar as a catalyst aligns with green chemistry rules by using renewable feedstocks and reducing waste production. Biochar can be functionalized with alkaline or alkaline earth metals to improve its basicity and catalytic activity.[20,21]

Many studies have shown how biochar-based catalysts can encourage transesterification reactions for GyC synthesis. For biochar production, researchers have examined different biomass sources, including agricultural residues (banana peels, oil palm ash), industrial waste (spent coffee grounds), and marine waste (mussel shells).[22] These materials are plentiful and cheap, which makes them good feedstocks for biochar production. Functionalized biochar catalysts from these sources have shown good success in experiments at the laboratory level, with high conversion rates and selectivity towards GyC.

For example, biochar from the calcined ash of *Mangifera indica* peel displayed excellent catalytic performance because it had a high basicity and could be reused.[23] Oil palm fuel ash and pyrolyzed fishery waste have also been used successfully as catalysts in transesterification reactions.[18] Other examples include spent coffee grounds combined with mussel shell ash and *Musa acuminata* peel ash, both of which showed promising results in terms of their catalytic efficiency and stability.[21,24] Even with these improvements at the laboratory level, there are still problems in expanding these processes for industrial uses.

This research aimed to develop and validate a scalable waste-derived catalytic platform for efficient glycerol to GyC upgrading, rather than merely optimizing reaction conversion. Specifically, a self-activated potassium-rich mesoporous biochar catalyst derived from banana bunch stalks (BS) was designed for GyC synthesis *via* transesterification with DMC. The BS are an abundant agricultural waste with a notable alkaline content, making them an attractive feedstock for producing intrinsically basic catalysts without external chemical impregnation. Previous studies have mostly worked to improve catalyst performance at the laboratory scale without addressing practical implementation challenges such as process scalability, product purification, and economic feasibility. In contrast, this research establishes an integrated framework combining catalyst design, reaction optimization, kinetic investigation, process simulation, and techno-economic analysis (TEA) to bridge the gap between laboratory research and industrial application. Response surface methodology (RSM) coupled with central composite design (CCD) was employed not only to optimize process parameters (catalyst loading, molar ratios of reactants, reaction temperature, and reaction time) but also to quantitatively evaluate parameter interactions and process intensification effects on GyC yield. In addition, kinetic modeling was performed to determine the reaction mechanism and apparent activation energy, providing mechanistic insight into the catalytic system. The long-term stability and ability to reuse the biochar catalyst was carefully tested. Furthermore, Aspen Plus-based process simulation was conducted to validate downstream separation feasibility and product purity at industrial scale, followed by a detailed TEA to determine commercial viability under realistic market conditions.

2. Materials and methods

2.1 Materials

The BS came from areas Songkhla, Thailand and were used as the raw material to prepare the biochar-based heterogeneous catalyst. Purified glycerol, as previously documented by Saetiao *et al.* (2025),[25] was utilized as the reactant. DMC (99% purity) was provided from Thermo Fisher Scientific Co., Ltd. Analytical-grade methanol (MeOH; 99.5% purity), used as a rinsing solvent to wash the catalyst after the reaction, was from RCI Labscan Limited. Isopropanol (99.5% purity), a solvent was from Loba Chemie™, India, while phenolphthalein was from Ajx Finechem Pty Ltd. Finally, 2,4-dinitroaniline and 4-nitroaniline, used as indicators, were supplied by Sigma-Aldrich Co. Ltd., USA.

2.2 Catalyst preparation

The BS were manually chopped into smaller pieces and thoroughly washed with distilled water to eliminate dust and surface impurities. The cleaned biomass was then dried in an oven at 105 °C overnight to remove any excess water. The dry material was then crushed into powder and passed through a 40-mesh sieve to provide a more uniform and finer particle size. The sieved powder then was placed into an alumina crucible and calcined in a tube muffle furnace at 700 °C under a steady flow of 100 mL min^{-1} of nitrogen (N_2) for 4 h. This allowed complete thermal breakdown of the organic

compounds, which included residual lignocellulosic components, based on prior methods.[26] This process would eventually generate a BS biochar (BSB) catalyst. The BSB contained metal oxides which acted as active sites during catalytic applications.[23] The prepared catalyst stayed in a desiccator to avoid reaction with atmospheric moisture and CO_2 before its use.

2.3 Catalyst characterization

2.3.1 Thermogravimetric analysis (TGA). The thermal stability and decomposition of the catalyst was determined *via* TGA using a PerkinElmer TGA8000 (USA) under a N_2 environment. Around 4 mg of dried sample was placed in an alumina pan and heated from 50 °C to 800 °C at 10 °C min^{-1} under a constant N_2 purging (flow rate of around 20 mL min^{-1}).

2.3.2 Surface area analysis. Using N_2 adsorption–desorption (ASAP2060 model, Micromeritics brand, USA), the Brunauer–Emmet–Teller (BET) specific surface area (S_{BET}) was evaluated, whilst the total pore volume (V_p), and average pore diameter were evaluated using the Barrett–Joyner–Halenda method from the desorption branch data, which was measured up to a relative pressure (P/P_0) of 0.99. Before the experiment, the sample was heated to 250 °C overnight under a vacuum condition to remove any surface water and volatiles from the sample.

2.3.3 Surface functional group analysis using Fourier-transform infrared spectroscopy (FT-IR). Surface functional groups in the catalyst were determined *via* FT-IR analysis (Bruker Vertex 70, Germany). The powdered sample was mixed together with potassium bromide, compressed into a pellet, and then analyzed for its infrared spectrum across a wavenumber from 4000–400 cm^{-1} at a spectral resolution of 4 cm^{-1}.

2.3.4 Phase composition and crystallinity analysis by X-ray diffraction (XRD). Phase composition and crystallinity of the catalyst was determined using wide-angle XRD analysis utilizing an Empyrean diffractometer (Netherlands) with CuKα radiation as the X-ray source. Diffraction patterns were collected over a 2θ range of 5–90° at a scan rate of 5° min^{-1}. The operating voltage and current were set to 40 kV and 30 mA, respectively. The average crystallite size of the catalyst was estimated using the Debye–Scherrer equation.

2.3.5 Morphological analysis. The morphological characteristics of the catalyst were examined through scanning electron microscopy (SEM; Hitachi SU3900, Japan) at 1500× magnification and an acceleration voltage equal to 15 kV to augment the image resolution and detailed surface features. The samples were coated with a thin gold film to improve conductivity and image quality. Energy-dispersive X-ray spectroscopy (EDX) was additionally used to analyze the elemental components.

2.3.6 pH analysis. The pH characterization of the synthesized catalyst was performed by preparing aqueous suspensions at 1 : 5, 1 : 10, 1 : 15, 1 : 30 and 1 : 40 weight : volume ratios of catalyst : distilled water. In each experiment, 1 g of catalyst was mixed with the required distilled water volume, ensuring uniform mixing. The pH was recorded using a waterproof handheld digital pH meter (150 & 450 series) to assure precision under various conditions.

2.3.7 Basic strength. The Hammett indicator method was used to evaluate the basic strength of the prepared catalyst. A 0.01 M benzoic acid solution in anhydrous MeOH acted as the titration medium in the determination of total basicity. The assessment utilized a series of Hammett indicators of known H_- values: bromothymol blue ($H_- = 7.2$), phenolphthalein ($H_- = 9.8$), 2,4-dinitroaniline ($H_- = 15.0$), and 4-nitroaniline ($H_- = 18.4$). The basic strength was inferred from the indicator color alteration.

2.4 Synthesis of GyC *via* transesterification

The synthesis of GyC by transesterification took place in a three-neck round-bottom flask with a reflux condenser to stop reactant loss. Cold water circulated continuously across the coil condenser to condense the DMC and MeOH vapors that then went back into the reaction mix to maintain the balance. A quantity of glycerol and DMC, measured with precision across different molar ratios (1 : 1 to 1 : 5) was added into the BSB catalyst (1–5 wt% relative to glycerol) and was continuously stirred at 500 rpm. The reaction proceeded at the given temperature (80 to 100 °C) and reaction time (60 to 180 min) by maintaining the flask within a silicone oil bath to provide precise thermal regulation. After the reaction, the flask was removed from the oil bath and cooled down to room temperature. The catalyst was then recovered through centrifugation at 4000 rpm for 20 min, while the unreacted DMC and MeOH byproducts were removed by vacuum distillation.

After the reaction, the recovered catalyst was thoroughly washed with MeOH to eliminate any lingering materials stuck to its surface, dried inside an oven at 105 °C overnight, and then stored for subsequent experimental trials.

Gas chromatography (Volare™), equipped with a flame ionization detector was used to analyze the composition of the reaction products with helium as the carrier gas and an Agilent HP-INNOWax capillary column (30 m × 0.25 mm × 0.25 μm). The injection volume was set at 1 μL and the injector and detector temperatures were maintained at 250 °C to facilitate efficient vaporization and detection of the analytes. Quantification of GyC and byproducts was performed using calibration curves prepared from standards of glycerol, dimethyl carbonate, and GyC. The GyC content in the final product was calculated based on calibrated peak areas in the chromatogram and its yield was calculated using eqn (1).

$$\text{Yield}(\%) = \frac{\text{GyC produced(moles)} \times 100\%}{\text{Glycerol in feed(moles)}}. \quad (1)$$

2.5 Experimental design and optimization using RSM-CCD

Optimization of the transesterification reaction to form GyC was evaluated using RSM with a CCD to systematically assess the effects of the four key process variables. RSM-CCD approach typically supports good optimization, minimizing the quantity of experiments needed during the transesterification process. Design Expert software (trial version 13, Stat-Ease, USA) helped build the experimental framework to analyze the influence of the reaction parameters on the GyC yield in order to find the optimal reaction conditions.

Table 1 Coded values of independent variables used in the central composite experimental design for optimizing GyC synthesis *via* transesterification

Variable	Value levels
A: DMC : glycerol molar ratio	1 : 1, 2 : 1, 3 : 1, 4 : 1, 5 : 1
B: Catalyst loading (wt%)	1, 2, 3, 4, 5
C: Reaction temperature (°C)	80, 85, 90, 95, 100
D: Reaction time (min)	60, 90, 120, 150, 180

Four separate variables served as factors affecting the transesterification process. These factors were the glycerol : DMC molar ratio (1 : 1 to 1 : 5), catalyst loading level (1–5 wt% relative to glycerol), reaction temperature (80–100 °C), and reaction time (60–180 min). These parameters directly influence active site availability, reaction equilibrium, and kinetic energy input in base-catalyzed transesterification systems. Within certain boundaries, these factors underwent alteration to measure their effects upon the reaction efficiency as summarized in Table 1. This CCD-based experimental design combined a full factorial arrangement, involving factorial, axial, and center points, to verify it as a robust statistical model. The equation $N = 2^n + 2n + 6$, where n stands for the quantity of separate variables, was used to fix the total number of experimental runs (N). With four factors, there were 27 experimental runs, which were comprised of 16 factorial points, eight axial points, and three center points. The experimental conditions and the matching response values were logged and assessed to create a predictive model for the transesterification reaction. The details can be found in Table 2.

A quadratic RSM aided assessment of the collected data, since it can show the nonlinear interactions within the process variables. The response variable (Y) was the GyC yield and followed a second-order polynomial equation (eqn (2));

$$Y = b_0 + \sum_{i=1}^{k} b_i X_i + \sum_{i=1}^{k} b_{ii} X_i^2 + \sum_{i=1}^{k} \sum_{j=i+1}^{k} b_{ij} X_i X_j + e, \quad (2)$$

where Y is the predicted response; X_i and X_j are the independent variables; b_0 is the interception; b_i, b_{ii}, and b_{ij} correspond to the regression coefficients for the linear, quadratic, and interaction terms, respectively; e captures random error, and k gives the total number of factors.

Through model accuracy and statistical importance were checked *via* analysis of variance (ANOVA). Further confirmation of the model came from examining the F-value, p-value, and coefficient of determination (R^2). The R^2 value close to 1 shows a good correlation and predictive ability. The F-value decided if the model differed much from pure error. An insignificant lack of fit confirmed the model explained the experimental data.

2.6 Process modeling

The production of biodiesel is a significant industry in Thailand, with each plant generating approximately 23 900 kg h^{-1}. This results in the production of 2390 kg h^{-1} of CG as a waste product.[27] To make better use of this waste CG, enrichment recovers about 60.84% of the glycerol to about 99.5% purity.[28] For this study, production capacities of 1500 kg h^{-1}, 3000 kg h^{-1}, and 4500 kg h^{-1} of enriched glycerol (99.5% purity) were selected based on experimental optimization. These capacities align with the requirements for downstream conversion into GyC, a high-value derivative. The GyC synthesis was simulated using Aspen Plus V11 software with the non-random two-liquid (NRTL) model being used to predict how the phases acted. Missing related factors came from the UNIFAC model, while the NRTL binary interaction factors suggested by Yu (2020)[29] were used. These made sure the thermodynamic predictions worked.

Table 2 Experimental results of the RSM-CCD for response surface analysis of GyC yield in the transesterification process

	Factors				GyC yield (%)		
Run	A	B	C	D	Actual	Predicted	Residual
1	+1	−1	+1	−1	57.88	59.29	−1.41
2	−1	−1	+1	+1	36.75	38.18	−1.43
3	−1	−1	−1	+1	60.03	58.97	1.06
4	0	0	0	0	91.86	91.94	−0.08
5	−1	+1	+1	−1	74.48	75.09	−0.61
6	+1	+1	−1	+1	92.16	95.87	−3.71
7	0	0	−2	0	93.16	95.19	−2.03
8	0	0	0	0	90.45	91.94	−1.49
9	+2	0	0	0	74.08	72.90	1.18
10	+1	+1	+1	−1	77.63	79.39	−1.76
11	+1	−1	−1	−1	52.77	52.78	−0.01
12	+1	−1	+1	+1	73.90	73.92	−0.02
13	0	0	+2	0	81.94	80.47	1.47
14	0	+2	0	0	70.11	69.06	1.05
15	−1	+1	+1	+1	42.41	43.10	−0.69
16	−1	−1	+1	−1	60.85	57.85	3.00
17	−1	+1	−1	−1	75.40	76.09	−0.69
18	+1	+1	+1	+1	82.23	81.69	0.54
19	−1	+1	−1	+1	67.07	64.34	2.73
20	−2	0	0	0	38.19	39.93	−1.74
21	+1	+1	−1	−1	76.02	73.32	2.7
22	0	−2	0	0	41.98	43.59	−1.61
23	0	0	0	+2	69.98	69.85	0.13
24	+1	−1	−1	+1	89.52	87.65	1.87
25	−1	−1	−1	−1	59.12	58.40	0.72
26	0	0	0	−2	66.28	66.97	−0.69
27	0	0	0	0	93.50	91.94	1.56

Table 3 Key assumptions applied in the TEA for GyC synthesis *via* transesterification using biochar-based green catalysts

Factors	Value	References
Lifetime of plant	20	25
Discount rate	7%	25
Incoming tax rate	20%	31
Start-up time, year	1	25
Construction duration, year	2	25
Operating period, days	330	25
Salvage value of % total capital investment cost	10	25
CEPCI in 2018	603.1	32
CEPCI in 2024	800	33

Table 4 CAPEX estimation method for the GyC synthesis process *via* transesterification using biochar-based green catalysts.[30]

Parameter	Value
Total purchase equipment cost (TPEC)	100% TPEC
Total direct cost	293% TPEC
Purchased-equipment installation	39% TPEC
Instrumentation and controls (installed)	13% TPEC
Piping (installed)	31% TPEC
Electrical systems (installed)	10% TPEC
Buildings (including services)	29% TPEC
Yard improvement	10% TPEC
Service facilities (installed)	55% TPEC
Land	6% TPEC
Total plant indirect costs	
Engineering and supervision	32% TPEC
Construction expenses	34% TPEC
Total contractor and contingency cost	
Contractors' fee	18% TPEC
Contingency	36% TPEC
Working capital investment	74% TPEC
Fixed capital investment (FCI)	Total direct cost + total plant indirect costs + total contractor and contingency cost
Total capital investment cost	FCI + working capital investment

The transesterification reaction to make GyC was patterned with prime conditions derived from experimental results with help from a CCD-assisted RSM. The BSB-based green catalyst was utilized to promote sustainable synthesis while minimizing environmental impact.

2.7 Techno-economic model

The economic feasibility of GyC synthesis *via* transesterification using the BSB catalyst was systematically evaluated for three feed capacities (1500 kg h^{-1}, 3000 kg h^{-1}, and 4500 kg h^{-1}) and the key economic assumptions, as summarized in Table 3. Equipment costs were updated to reflect 2024 values using the chemical engineering plant cost index (CEPCI). The CEPCI amounts were 603.1 for 2018 and 800 for 2024, as shown in eqn (3),

$$C_{\text{updated}} = C_{\text{reference}} \times \frac{\text{CEPCI}_{2024}}{\text{CEPCI}_{2018}}. \quad (3)$$

All equipment was assumed to be constructed from stainless steel to enhance corrosion resistance and ensure operational longevity. The capital expenditure (CAPEX) calculations included total purchased equipment cost, total direct costs, total plant indirect costs, contractor and contingency costs, and working capital investment. Those parts were summed to yield the total capital investment, as outlined in Table 4.[30] Operational expenditure (OPEX) was derived from substances besides energy balances using the Aspen Plus software, and incorporated raw material prices, utility costs, and fixed expenses, such as labor and maintenance, as summarized in Table 5.

Key performance indicators were employed to assess the profitability of the process across different plant sizes. Net present value (NPV) was calculated using discounted cash flow analysis over a plant lifetime of 20 years at a discount rate of 7%, as shown in eqn (4);

$$\text{NPV} = \sum_{t=1}^{n} \frac{R_t}{(1+i)^t}, \quad (4)$$

where R_t equals net cash flow in year t, i equals the discount rate, and n equals years of work. The internal rate of return (IRR) appeared from cutting the discount, so NPV equaled zero, as shown in eqn (5):

$$\text{NPV} = 0 = \sum_{t=0}^{n} \frac{\text{CF}_t}{(1+\text{IRR})^t}, \quad (5)$$

Payback period (PBP) was calculated using eqn (6),

$$\text{PBP} = \frac{\text{cost in investment}}{\text{annual net cash flow}}. \quad (6)$$

Sensitivity analysis was conducted to account for economic uncertainties by varying key parameters, such as equipment costs, utility prices, GyC selling price, and enriched glycerol cost. This study offers a detailed techno-economic framework for scaling up GyC production using biochar-based catalysts while addressing market dynamics and sustainability goals in chemical manufacturing processes.

3. Results and discussion

3.1 Catalyst characterization

3.1.1 TGA analysis. The thermal decomposition behavior of the BSB catalyst was examined by TGA and its derivative

Table 5 Operating cost estimation for the GyC synthesis

Component of operating cost	Estimated price	References
Variable production costs		
Raw materials		
Enriched glycerol (99.5%)	0.560 (USD per kg)	34
DMC	1.000 (USD per kg)	27
Aniline	1.840 (USD per kg)	35
Catalyst	5.000 (USD per kg)	36
Products		
GyC	3.500 (USD per kg)	37
Utilities		
Steam (LPS)	10.69 (USD per GJ)	38
Steam (MPS)	13.28 (USD per GJ)	38
Steam (HPS)	15.73 (USD per GJ)	38
Cooling water	0.354 (USD per GJ)	38
Electricity	0.084 (USD per kWh)	31
Waste disposal	200 (USD per ton)	39
Fixed costs		
Labour cost	(6 Persons) specialized engineering, $13 548 per year (12 Persons) technical staff, $18 580 per year (6 Persons) maintenance engineering, $7742 per year (3 Persons) secretary, $11 612 per year	40
Operating supplies	0.5% of FCI	30
Maintenance and repairs	2% of FCI	30
Laboratory expenses	10% of labour cost	30
Patents and royalties	1% of FCI	30
Local taxes	1% of FCI	30
Insurance	0.4% of FCI	30
Plant-overhead costs	5% of TPC	30
Administrative costs	5% of TPC	30
Distribution and selling costs	1% of TPC	30
Total product cost (TPC) = raw materials + utilities + fixed cost		

thermogravimetric (DTG) profile over a temperature range from 50 °C to 800 °C (Fig. 1a), with the data also being used to determine the temperature for calcination.

The initial stage at 100 °C and 258 °C resulted in a small mass loss (about 10.12%), mostly from residual moisture evaporation and physically adsorbed water release. The DTG peaks (Fig. 1b) confirmed this, showing that moisture removal remained the dominant event within this temperature range. During the next phase, from 258 °C to 452 °C, a considerable mass loss of approximately 47.11% was noted, which represents the thermal degradation of organic components, like hemicellulose and cellulose, and the loss of volatile compounds.[41] Notably, the DTG curve revealed that the maximum decomposition rate occurred at 271 °C, marking the peak thermal instability of the material, beyond which a rapid degradation of lignocellulosic and cellulose constituents was observed. From 452 °C to 800 °C, the material went into a third degradation phase accounting for an additional weight reduction of 7.61%, representing biochar formation and the gradual decomposition of carbonous material.[23] Thereafter, higher temperatures gave a stable weight loss, representing a stable calcination process where much of the organic matter was decomposed and an ash-rich residue remained. This residue has a critical function in the catalytic properties. From these observations, the calcination temperature of the BS was set at 700 °C to prepare the BSB catalyst to ensure the material kept its structural integrity.

3.1.2 Surface area analysis. The S_{BET} of the synthesized catalyst was only 1.26 $m^2\ g^{-1}$, which indicates a low surface area. This may be attributed to the low presence of uncharred carbon particles within the biochar matrix, which limits the formation of an extensive porous network.[42,43] Despite having a modest surface area, the catalyst was found to have a remarkable catalytic efficiency, which reflects its high potassium content and, consequently, strong basicity. At a relative pressure (P/P_0) of 0.990, the V_p was 0.006274 $cm^3\ g^{-1}$, supporting a well-developed mesoporous framework that is good for reactant diffusion and product desorption.[44] Moreover, the N_2 adsorption–desorption isotherm of the BSB catalyst (Fig. 2a) displays a type IV isotherm, supporting it as a mesoporous material with defined pores. Calcination decreased the S_{BET} and V_p, which reflects the structural changes in the biochar due to thermal sintering and partial agglomeration to form a more

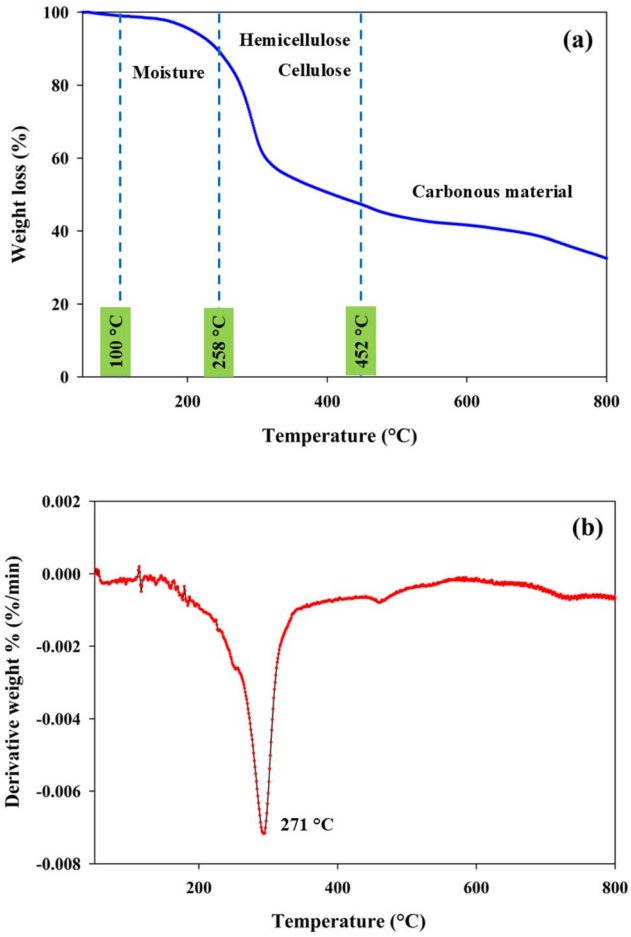

Fig. 1 (a) Thermogravimetric analysis and (b) derivative thermogravimetric thermograms of banana bunch stalk biochar.

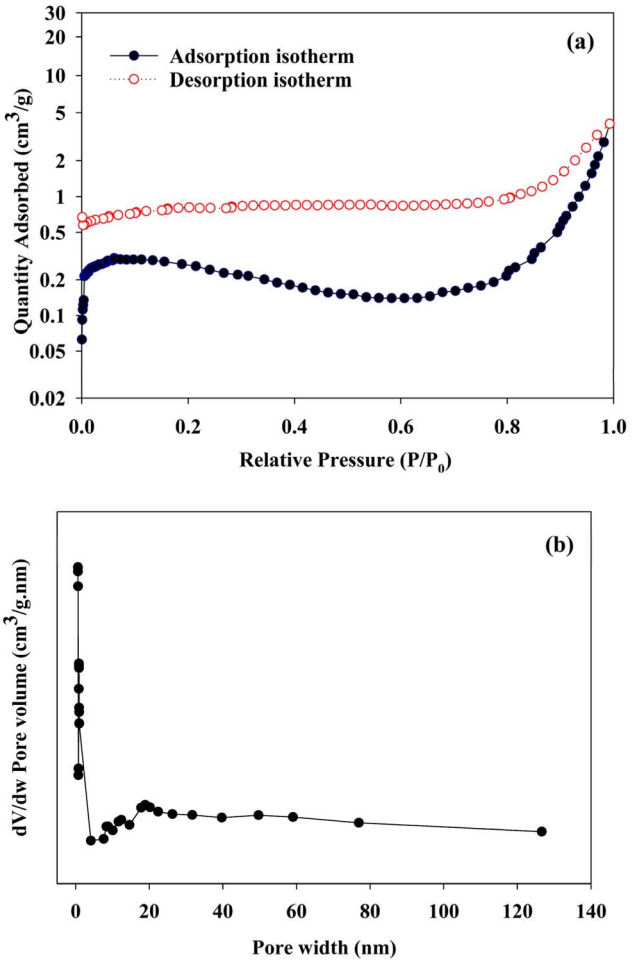

Fig. 2 (a) Representative Brunauer–Emmett–Teller surface area analysis and (b) BJH pore-size distributions of banana bunch stalk biochar.

compact structure. The average pore diameter was 19.9 nm (Fig. 2b), making the BSB catalyst mesoporous, since mesoporous structures usually have pores within the 2–50 nm range.

3.1.3 Functional group analysis (FT-IR). Functional groups in the BSB catalyst were characterized by FT-IR spectroscopy across a range of 4000–400 cm^{-1}. The findings confirmed key functional groups linked to its catalytic action, as shown in Fig. 3. The broad absorption band around 3448.7 cm^{-1} was ascribed to O–H stretching vibrations from the hydroxyl groups of lignocellulosic components. Absorption peaks at 1121.8 cm^{-1} and 1015.6 cm^{-1} matched C–O stretching and bending vibrations from the functionalized oxygenated groups on the catalyst surface.[45] Notably, peaks at 866.7, 706.1, 670.6, and 620.3 cm^{-1} relate to O–H bending vibrations from adsorbed water molecules. Thus, the catalyst retains or absorbs moisture in the lab environment. The clear peak at 1645.3 cm^{-1} is ascribed to the stretching and bending vibrations of carbonate groups, namely K_2CO_3,[46] and reflects the active alkaline species present within the catalyst that play a key role in its basicity and catalytic performance. A sharp absorption band at 1400.3 cm^{-1} verified the presence of K_2CO_3 species in the catalyst.[26,47] The well-defined nature of this peak suggests the fresh catalyst has a stable distribution of basic sites.

3.1.4 Structural analysis (XRD). The structural characteristics and crystalline phases of the BSB catalyst were investigated using XRD over a 2θ scan range from 10° to 90°. The XRD profile (Fig. 4) showed a few clear diffraction peaks. The most intense peaks near 28.37° and 49.60° were likely due to the presence of potassium chloride (KCl).[48] Additionally, several diffraction peaks were observed at 19.95°, 38.67°, 40.53°, 41.64°, 58.65°, and 66.38°, corresponding to tetragonal crystalline structures of potassium. The presence of these peaks shows that potassium compounds formed the main phase in the biochar matrix. As a result, its catalytic activity would be higher because they would act as active sites in transesterification and other chemical reactions. A notable diffraction peak was present at a 2θ of 29.69°, which is characteristic of K_2CO_3. Overall, this supports that potassium existed in large amounts inside the catalyst structure.[49] Other diffraction peaks at 25.78°, 41.33°, 42.50°, and 49.60° were assigned to potassium oxide (K_2O).[46] These results match prior studies, such as that by Jitjamnong *et al.* (2021), which reported related crystalline structures based on potassium in banana peel biochar catalysts utilized for biodiesel creation.[26] The potassium phases have great importance, because they play

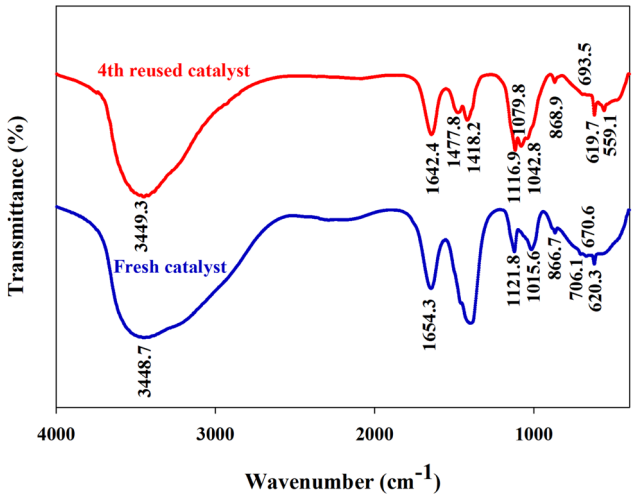

Fig. 3 Representative Fourier-transform infrared spectroscopy spectra of the fresh and 4th reused banana bunch stalk biochar catalyst.

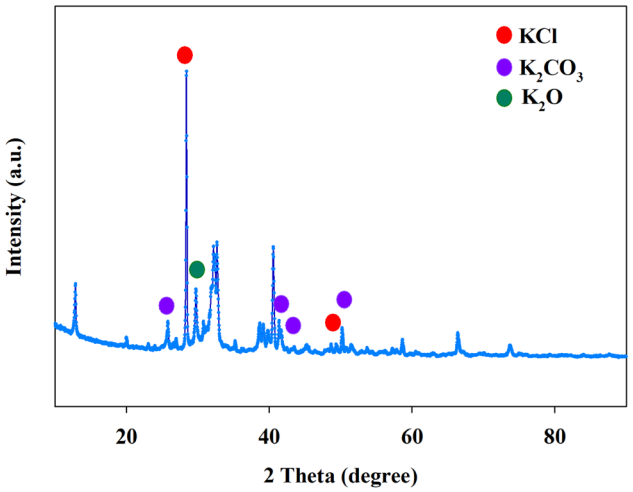

Fig. 4 Representative X-ray diffraction pattern of banana bunch stalk biochar.

a key role in raising the catalytic power of the biochar. This could be useful for many heterogeneous catalytic applications. The Debye–Scherrer equation was used to estimate the crystallite size of the biochar catalyst, giving a particle size of around 38.42 nm. This small size helps with catalytic applications, since it adds to the surface area and also raises the reactivity and power in transesterification and other chemical processes.

3.1.5 Morphology and elemental composition (SEM-EDX analysis). The morphology and elemental makeup of the catalyst was evaluated *via* SEM-EDX analysis. The catalyst was first calcined at 700 °C, resulting in a coarse surface that was not even, including many voids and structural changes (Fig. 5a). This morphology suggests a lack of a well-developed porous network, which may be attributed to the non-porous nature of the precursor biomass. This is consistent with the pore size distribution analysis that revealed an average pore diameter of 19.9 nm, but the V_p was relatively low, which is consistent with the limited development of an extensive porous network. However, the presence of aggregated structures showing mesoporous features may increase the catalytic power in certain reactions.

The elemental distribution, derived from the EDX analysis (Fig. 5b and c), showed that potassium (K), oxygen (O), and carbon (C) were the main elements present, with phosphorus (P), calcium (Ca), silicon (Si), sulfur (S), and chlorine (Cl) being present in small amounts. Because potassium has value as a basic catalyst, its large presence hints that the catalyst has strong alkaline traits, which are key for transesterification reactions. The high basic strength of potassium and its reactivity with water backs its potential to work as a catalyst.[50,51]

3.1.6 pH analysis. The BSB catalyst displayed strong alkaline traits. The pH value decreased with increasing catalyst dilution (Fig. 6), being highest (pH 13.36) at a 1 : 5 (w/v) ratio of catalyst : water and then decreasing to pH 12.43 at a 1 : 40 (w/v) ratio, reflecting the reduction in the active basic compound concentrations with lower catalyst dilutions. The high alkalinity suggests the potential as a good basic catalyst, such as for transesterification reactions.

3.1.7 Basicity analysis. The basicity and basic strength of the BSB-based catalyst were determined using the Hammett indicator method. The fresh catalyst had a total basicity of 3.66 mmol g^{-1} indicating a high density of accessible basic active sites. This basicity was primarily attributed to potassium-containing species, particularly K_2CO_3 and K_2O phases formed during pyrolysis, which contribute significantly to the catalyst alkaline nature and catalytic efficiency.

The fresh catalyst basic strength ($H\_$) was determined to lie within the range of $9.8 < H\_ < 15$, as evidenced by a color change with phenolphthalein ($H\_ = 9.8$) but no change with indicators of higher basic strength. This indicates the presence of moderately strong basic sites sufficient to promote base-catalyzed transesterification reactions efficiently. These findings are consistent with the high alkaline pH (Section 3.1.6) and potassium levels (Section 3.1.5), confirming that intrinsic potassium species are the dominant contributors to the observed basicity and catalytic performance of the BSB catalyst.

3.2 Statistical and RSM analysis

ANOVA analysis of the GyC synthesis was performed to evaluate the statistical significance and adequacy of the model. The quadratic polynomial model developed for GyC synthesis, shown as (eqn (7)), demonstrated strong statistical validity and predictive capability for the experimentally obtained GyC yields (Table 6). The high *F*-value (93.18) and low *p*-value (less than 0.0001) indicate that the model is reliable. These values confirm that the model adequately captures the relationships among the reaction parameters. The coefficient of determination (R^2 = 0.9909) shows that the model explains over 99% of the variability in experimental outcomes. Such a high R^2 value is consistent with previous reports on base-catalyzed transesterification systems, where high R^2 values verified the effectiveness of RSM for optimizing systems with several to many

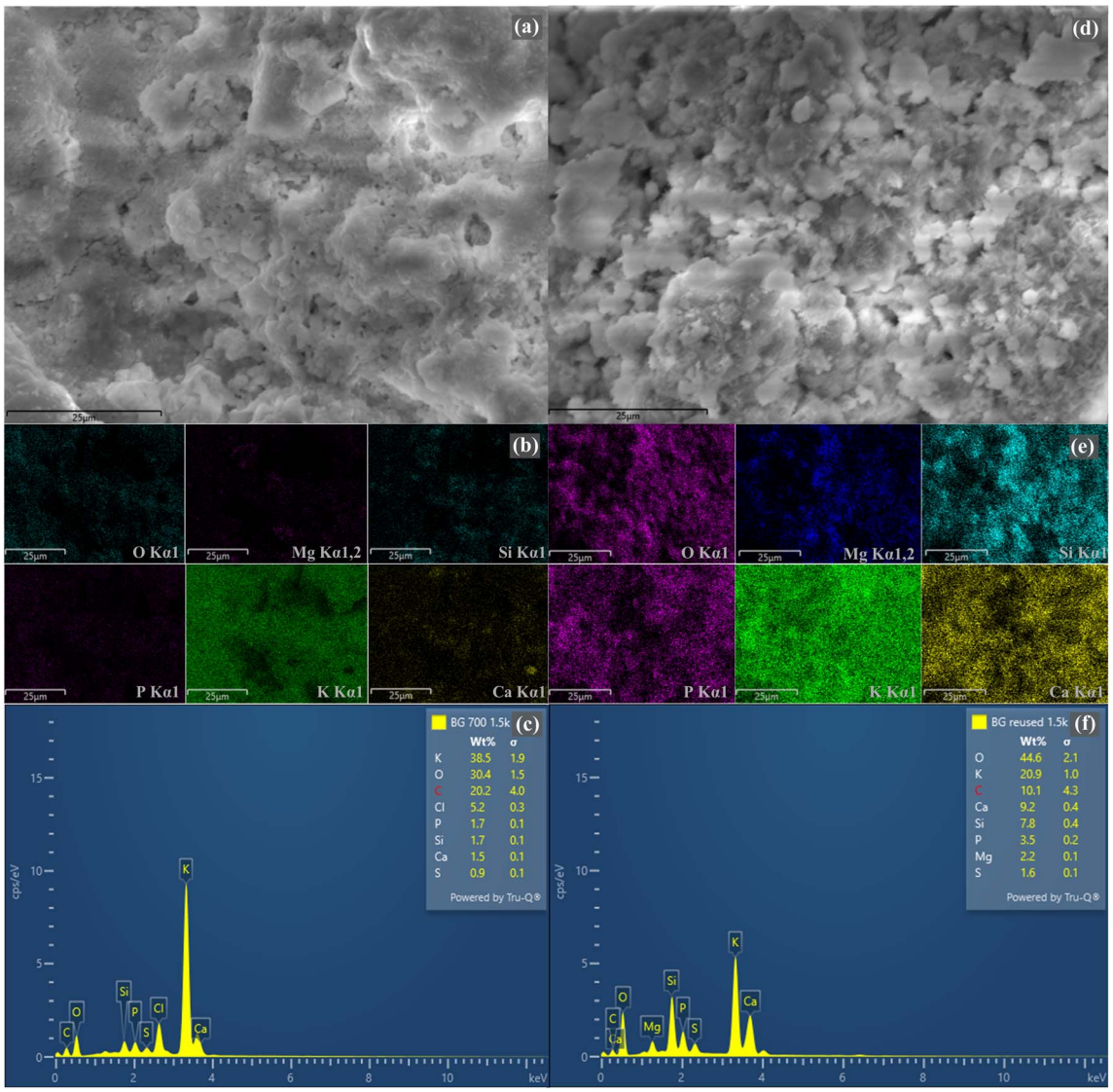

Fig. 5 Representative SEM images (1500×) of banana bunch stalk biochar: (a) surface morphology; (b) EDX spectrum for elemental composition; (c) elemental mapping. Panels (d–f) show reused catalysts: (d) SEM, (e) EDX, and (f) elemental mapping, highlighting structural and compositional changes after reuse.

variables.[12,52] In this study, the interactions between factors and quadratic terms were also evaluated to obtain deeper information about non-linear effects, which is essential for accurately defining optimal operating windows for potential scale-up.

Among the linear terms, the DMC to glycerol molar ratio (A) and catalyst loading (B) were identified as the most significant factors (p-value < 0.0001). Both variables also exhibited significant quadratic effects (A^2 and B^2), confirming the presence of curvature in the response surface. Reaction temperature (C) showed a statistically significant linear effect, while reaction time (D) was not significant as an individual linear term (p = 0.1720), indicating that within the investigated range, its direct influence is comparatively weaker.

The interaction between DMC to glycerol molar ratio and reaction time (AD) was highly significance (F-value = 199.55), indicating a strong synergistic influence on GyC yield. Mechanistically, increasing the DMC : glycerol molar ratio shifts the reaction equilibrium toward GyC formation, while sufficient reaction time allows the system to approach equilibrium. At lower molar ratios, longer reaction times are required to achieve comparable conversion, whereas at higher molar ratios, equilibrium is reached more rapidly. This explains the strong statistical significance of the AD interaction term.[53,54]

The lack-of-fit test gave a p-value of 0.2889, revealing that there is no significant difference between the model predictions and experimental data at a 95% confidence level, thereby confirming that the quadratic polynomial model describes the experimental system. This indicates that the model is neither overfitted nor excessively complex. The high adequacy precision (31.8847) validated the model predictive ability, confirming a strong signal-to-noise ratio well above the desirable threshold of 4. By excluding non-significant terms, such as the AB and BC

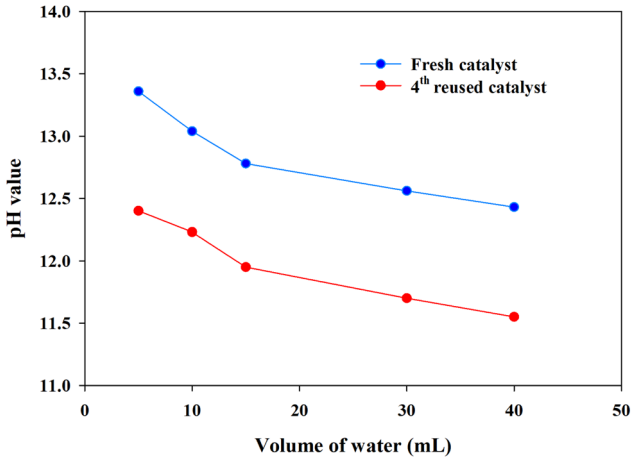

Fig. 6 pH values of banana bunch stalk biochar (fresh catalyst) and the 4th reused catalyst at varying water dilution volumes.

interactions, the model compromises between complexity and accuracy. Facilitating practical implementation without compromising predictive accuracy. This approach improves the optimization process and meets sustainability goals by reducing the number of experiments and the use of resources. Since GyC has gained recognition as a value-added product in biorefinery uses, this study creates a strong structure for increasing GyC production while ensuring environmental and economic sustainability.[53,55] The developed model demonstrates high predictive reliability and provides mechanistic insight into the interaction effects among process variables, as expressed in (eqn (7)).

$$\text{GyC yield (\%)} = 91.94 + 8.24A + 6.37B - 3.68C + 0.7196D + 0.7131AB + 1.77AC + 8.57AD - 0.1119BC - 3.08BD - 0.56CD - 8.88A^2 - 8.90B^2 - 1.03C^2 - 5.88D^2. \quad (7)$$

Comparison of the experimental and predicted values for the GyC yield (Fig. 7a) reveals the sturdiness and precision of the quadratic polynomial model. The strong agreement between predicted and experimental data further confirms the validity of the selected process parameters and the adequacy of the statistical model. Thus, the model can capture the relationship between input variables and output response in a dependable manner.

The random distribution of data points around the diagonal line in the parity plot confirms the absence of systematic prediction errors. This indicates that the model effectively accounts for experimental variability. The lack of curvature or obvious patterns in the residuals confirms that the quadratic polynomial model is suited for describing the system as it accurately represents the linear and non-linear effects of the process parameters on the GyC yield.

The perturbation plot (Fig. 7b) shows a visual picture of how sensitive the GyC yield is to changes in key process parameters. This plot allows for a comparative analysis of the individual impact of each factor on the GyC yield while keeping the other parameters constant at their optimal levels. The reference point shows the central values for the CCD experimental design.

Among the four factors, catalyst loading revealed the largest curvature and so has a crucial role in influencing the GyC yield. This observation is consistent with the ANOVA results identifying catalyst loading and DMC : glycerol molar ratio as the

Table 6 ANOVA for the quadratic polynomial model of GyC synthesis *via* transesterification using biochar-based green catalysts

Source	Sum of squares	Degree of freedom	Mean square	*F*-value	*p*-value
Model	7685.54	14	548.97	93.18	<0.0001
Linear					
A	1630.70	1	1630.70	276.79	<0.0001
B	972.70	1	972.70	165.10	<0.0001
C	325.24	1	325.24	55.20	<0.0001
D	12.43	1	12.43	2.11	0.1720
2-Way interaction					
AB	8.14	1	8.14	1.38	0.2627
AC	49.88	1	49.88	8.47	0.0131
AD	1175.63	1	1175.63	199.55	<0.0001
BC	0.2003	1	0.2003	0.0340	0.8568
BD	151.84	1	151.84	25.77	0.0003
CD	409.76	1	409.76	69.55	<0.0001
Square					
A^2	1682.35	1	1682.35	285.55	<0.0001
B^2	1690.88	1	1690.88	287.00	<0.0001
C^2	22.48	1	22.48	3.82	0.0745
D^2	737.98	1	737.98	125.26	<0.0001
Residual	70.70	12	5.89		
Lack of fit	66.04	10	6.60	2.83	0.2889
Pure error	4.66	2	2.33		
Total	7756.23	26			

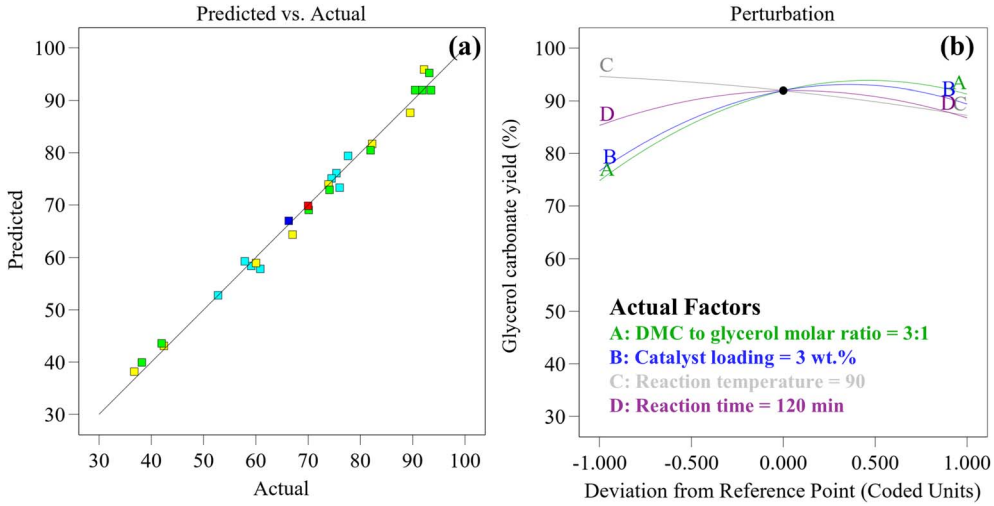

Fig. 7 Model evaluation for GyC yield: (a) correlation plot of predicted *vs.* actual yields, and (b) perturbation plot showing the effect of process variables on yield.

most statistically significant factors ($p < 0.0001$). The steep curve suggests that slight changes can result in large changes in the GyC yield. The DMC : glycerol molar ratio also demonstrated high sensitivity, reinforcing its critical role in shifting reaction equilibrium and maximizing conversion. In contrast, reaction temperature displays medium effects on the GyC yield. The reaction time displayed a relatively flatter curve, consistent with its non-significant *p*-value (0.1720) in the ANOVA analysis. Therefore, within the investigated range, variations in reaction time exert a comparatively small influence on the GyC yield.

3.3 Interaction effects on GyC synthesis

The 3D plots (Fig. 8) show how the interaction of pairs of factors affect the GyC yield. The effects of two factor interactions on the transesterification GyC yield are discussed in Sections 3.3.1 to 3.3.6.

3.3.1 Effect of the DMC : glycerol molar ratio and catalyst loading (AB). The 3D contour plot displays the interaction between the DMC : glycerol molar ratio and catalyst loading (wt%) on the GyC yield is shown in Fig. 8a. Both the catalyst loading and the DMC : glycerol molar ratio significantly influenced the GyC yield, as supported by their high *F*-values and low *p*-values (<0.0001) in the ANOVA results (Table 6). Increasing the catalyst loading from 2 to 4 wt% strongly enhanced the GyC yield, underscoring the critical function of the catalyst in the transesterification procedure. This improvement results from there being more active sites, which speeds up the reaction rate[12] and so increases the rate of product formation. Increasing the catalyst loading above 4 wt% gives smaller returns, presumably because the excess basic active sites saturate the reaction system allowing unwanted side reactions, like GyC transformation into glycidol.[24] These side reactions can reduce the total efficiency and selectivity of the process.

The DMC : glycerol molar ratio showed a strong positive effect on the GyC yield, with an optimal ratio at around 3 : 1. This is in accord with past work that showed increasing the proportion of DMC up to its optimal level pushes the equilibrium-limited reaction forward and so raises product formation.[56] However, beyond the optimal ratio, a gradual decline in GyC yield was observed. This behavior confirms the negative quadratic coefficient (A^2) in the model, indicating the presence of a true optimum rather than a continuously increasing trend. Excess DMC may dilute the effective glycerol concentration near the catalyst surface and potentially promote side or reversible reactions, thereby reducing the overall conversion efficiency.[57,58] The interaction term *AB* did not have any statistical significance ($p = 0.2627$), as seen by the contour lines that look smooth without sharp bends or oddities. Thus, both factors increase the GyC yield on their own without any synergistic or antagonistic interactions within the range tested.

3.3.2 Effect of the DMC : glycerol molar ratio and reaction temperature (*BC*). The interaction effect is evident in the curvature of the contour lines (Fig. 8b), suggesting that the impact of one factor is dependent on the level of the other. At lower reaction temperatures (85–89 °C), raising the DMC : glycerol molar ratio from 2 : 1 to 3 : 1 resulted in a moderate gain in the GyC yield. However, at higher temperatures (91–95 °C), the same increase in the DMC : glycerol molar ratio led to a more pronounced enhancement in the GyC yield, indicating a synergistic relationship between these two variables.

Reaction temperature is a key parameter that shapes both the kinetics and thermodynamics of GyC synthesis. High temperatures enhance the reaction rates by increasing molecular collisions and easing the removal of protons from glycerol. Glycerol reacts with DMC to create GyC.[14] The plot suggests that under ideal conditions, reaction temperatures may help give GyC yields as high as 93–95%, particularly when paired with an optimal DMC : glycerol molar ratio. However, excessively high temperatures may promote side reactions or thermal decomposition of intermediates and products,[59] thereby reducing GyC selectivity. Such undesired reactions may also increase by-product formation, complicating downstream purification.

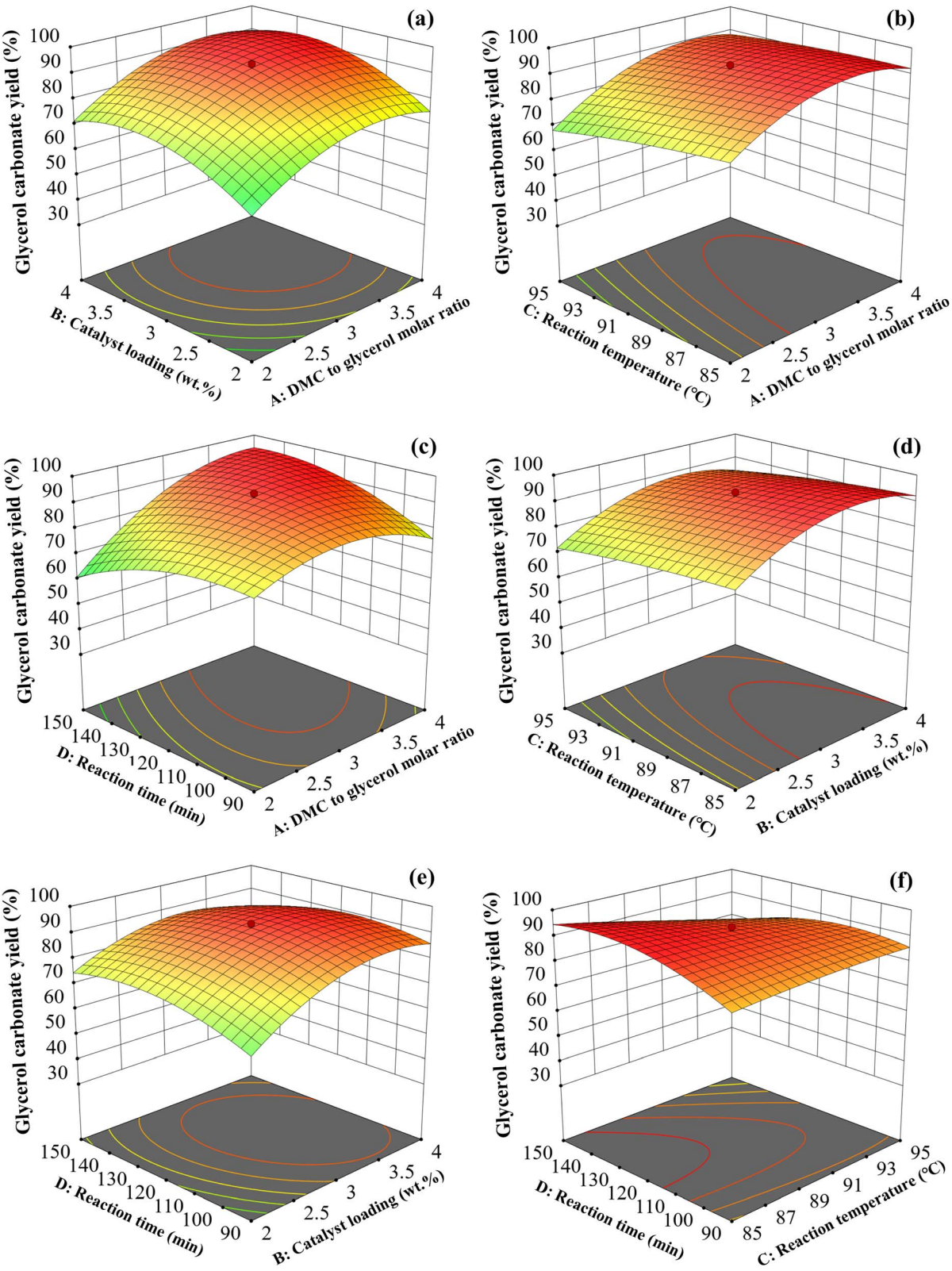

Fig. 8 3D surface plots showing how pairs of process variables affect the GyC yield: (a) DMC : glycerol ratio and catalyst loading, (b) DMC : glycerol ratio and temperature, (c) DMC : glycerol ratio and time, (d) catalyst loading and temperature, (e) catalyst loading and time, and (f) temperature and time.

This trend is consistent with the ANOVA results, where reaction temperature was identified as a statistically significant factor ($p < 0.0001$; F-value of 55.20), and the negative quadratic coefficient (C^2) further confirms the existence of an optimal temperature rather than a continuously increasing trend. Therefore, precise temperature control is essential to maximize GyC yield while preventing efficiency losses due to thermal side reactions.

3.3.3 Effect of the DMC : glycerol molar ratio and reaction time (*BD*). The interaction effect between the DMC : glycerol molar ratio and reaction time on the GyC yield is shown in Fig. 8c. At shorter reaction times (90–110 min), raising the DMC : glycerol molar ratio from 2 : 1 to 3 : 1 gave moderate gains in the GyC yield. This results from the limited time in which the reactants must beat mass transfer resistance and reach all the catalyst active sites.[57] As the reaction time reaches 120–140 min, the same boost in the DMC : glycerol molar ratio gave a more marked enhancement in the GyC yield. The longer reaction period gives enough time for mass transfer limits to fade, thus letting the excess DMC push the equilibrium toward GyC formation. This is in accord with the ANOVA study where the *AD* interaction term had a high statistical significance (F-value = 199.55, $p < 0.0001$). This stressed how important it is to consider both parameters at once during process improvement. Very long reaction times or high DMC : glycerol molar ratios over 3 : 1 leads to smaller returns or wasted resources, as seen in the flattening of the contour lines at extreme values.

3.3.4 Effect of catalyst loading and reaction temperature (*AC*). The interaction between the catalyst loading level and reaction temperature is shown in Fig. 8d. At lower catalyst loadings (1–2 wt%), increasing the reaction temperature from 85 °C to 90 °C caused a moderate increase in the GyC yield, but was much higher at higher catalyst loadings (3–4 wt%). This hints at a synergistic link between these two variables, which likely comes from the increased number of active sites at higher catalyst loadings, whilst increased temperatures speed up the reaction kinetics and so also improve the GyC yield. The ANOVA study supports an interaction between these two factors with a statistically significant AC interaction term (F-value = 8.47, $p = 0.0131$). Thus, although both factors alone help increase the GyC yield, their combined effect becomes a key determinant in the GyC yield. Too high a catalyst loading or reaction temperature (above their respective optimal value) can result in a smaller increase in the GyC yield due to the promotion of unwanted side reactions.

3.3.5 Effect of catalyst loading and reaction time (*AD*). The interaction between the catalyst loading and reaction time is shown in Fig. 8e. At lower catalyst loadings (2–2.5 wt%), increasing the reaction time from 90 to 120 min gave moderate gains in the GyC yield, whereas at higher catalyst loadings (3–4 wt%), the same increase in the reaction time results in a more marked enhancement of the GyC yield. This might reflect that the enhanced level of active catalytic sites at higher catalyst loadings require sufficient reaction time to fully facilitate the transesterification process. In accord, the ANOVA results show the *AD* interaction has a very high significance (F-value = 25.77, $p = 0.0003$) and so their combined effect notably affects the GyC yield. Too high a catalyst loading or too long a reaction time above their respective optimal range leads to smaller GyC enhancements or operational waste, as reflected by the flattening of contour lines at extreme values.

3.3.6 Effect of the reaction temperature and reaction time (*CD*). The 3D contour plot of the effect of the reaction temperature and reaction time on the GyC yield is shown in Fig. 8f. At lower reaction temperatures (85–90 °C), increasing the reaction time from 90 to 120 min led to moderate gains in the GyC yield, whereas at higher temperatures (90–95 °C), the same increase in the reaction time leads to a more marked GyC yield enhancement. The higher temperatures speed up the reaction kinetics which allows the extended reaction time to work better at pushing the equilibrium toward GyC. In accord, the CD interaction term shows a high F-value (69.55) and low p-value (<0.0001), supporting that the combined effect of reaction temperature and reaction time plays a key role in shaping the GyC yield. Higher temperatures or longer reaction times may lead to side reactions or thermal decay, as seen in the flattening of the contour lines at extreme value indicates this.

3.4 Optimization of GyC synthesis

A combination of CCD with RSM was used to optimize the GyC synthesis, where this combination gave a precise control of key reaction parameters (Fig. 9). The theoretical optimal conditions for GyC synthesis were a DMC : glycerol molar ratio of 3.58 : 1, a catalyst loading of 3.45 wt%, a reaction temperature of 90.20 °C, and a reaction time of 119 min. Under those conditions, the predicted GyC yield was 94.77%, which was near the actual obtained experimental yield of 92.40%. The percentage deviation between the predicted and experimental yields was found to be 2.56%, indicating excellent agreement between model prediction and experimental validation. Along with the close match between the predicted an experimental GyC yields across all 27 tested conditions (Table 2), where deviation values were consistently within an acceptable range, this points to the accuracy, robustness, and reliability of the RSM-CCD optimization approach.

3.5 Kinetic study

The transesterification of glycerol with DMC to synthesize GyC follows a complex reaction mechanism that can be effectively described using the Langmuir–Hinshelwood–Hougen–Watson (LHHW) model. This model states that the catalyst surface drives the process through a dual-site process. For transformation to occur, both reactants must undergo adsorption.[60] The surface reaction controls the reaction rate rather than diffusion. Thus, the catalytic surface process determines the overall reaction kinetics. Because both glycerol and DMC seek available active sites on the catalyst surface, they engage in competitive adsorption, thereby influencing each other's surface coverage. The adsorption behavior of the reactants follows the Langmuir isotherm, implying that the extent of adsorption is proportional to the reactant concentration until surface saturation is reached. However, this reaction is not close to equilibrium, because the reverse reaction is insignificant. Thus, a simplified kinetic model can focus on the forward

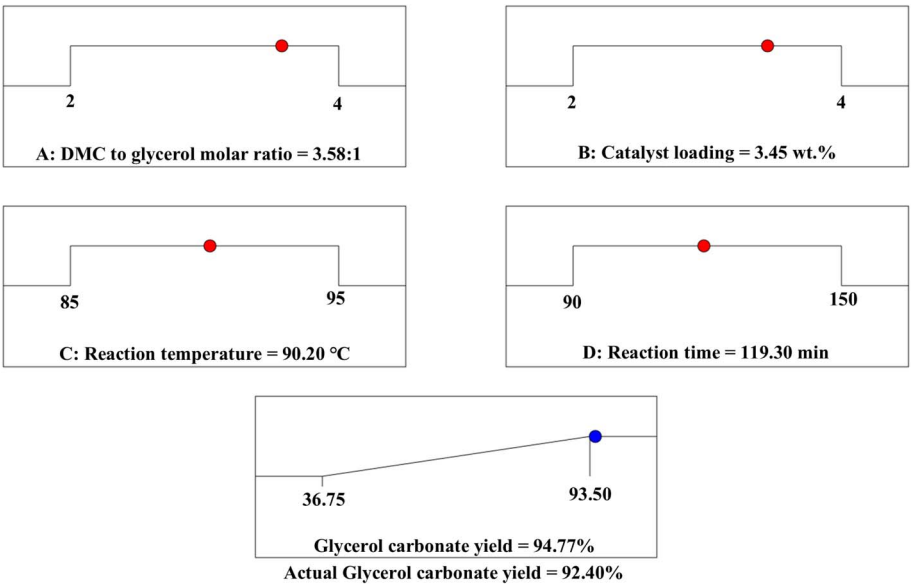

Fig. 9 Ramp desirability plot for numerical optimization of GyC synthesis using RSM-CCD.

transesterification direction. These assumptions collectively provide a robust framework for modeling and optimizing the catalytic conversion of glycerol to GyC (eqn (8)).

$$\text{Glycerol} + \text{DMC} \rightarrow \text{GyC} + \text{MeOH}, \tag{8}$$

According to the LHHW model, the rate equation for this reaction can be expressed as (eqn (9) and (10))

$$r = k\frac{K_G C_G}{(1 + K_G C_G + K_D C_D)}\frac{K_D C_D}{(1 + K_G C_G + K_D C_D)}, \tag{9}$$

$$r = \frac{kK_G K_D C_G C_D}{(1 + K_G C_G + K_D C_D)^2}, \tag{10}$$

where the reaction rate (r) is expressed in units of mol L^{-1} min^{-1} and the temperature influences the reaction rate constant (k). The concentrations of glycerol (C_G) and DMC (C_D) influence the reaction rate. Glycerol and DMC adsorption equilibrium constants (K_G and K_D, respectively) describe the attraction strength between these reactants and the catalyst surface. Because reactants have weak adsorption, the denominator terms $K_A C_A$ and $K_B C_B$ are far below 1, allowing the approximation $1 + K_G C_G + K_D C_D$ to be near to 1. Thus, the rate equation simplifies to (eqn (11)),

$$r = kC_A C_B. \tag{11}$$

If one reactant, B is in large excess, its concentration remains nearly constant, allowing the rate law to be rewritten as an apparent first-order reaction with respect to A (eqn (12)):

$$r = k' C_A, \tag{12}$$

where $k' = kC_B$.

Thus, for a first-order reaction, the differential rate equation is (eqn (13))

$$\frac{dC_A}{dt} = -k' C_A. \tag{13}$$

Separating variables and integrating we get (eqn (14)):

$$C_A = C_{A,0} e^{-k't}. \tag{14}$$

Thus, the final expression for conversion is (eqn (15)):

$$X = 1 - e^{-k't}. \tag{15}$$

To investigate the reaction kinetics over BSB, experiments were conducted at three temperatures (85, 90, and 95 °C) and four reaction durations (60, 90, 120, and 150 min), while maintaining the DMC : glycerol molar ratio (3.58 : 1) and catalyst loading (3.45 wt%) at their optimized values. The experimental data (Fig. 10a) demonstrated excellent agreement with the pseudo-first-order kinetic model, indicating that reaction rate depends primarily on glycerol concentration under the studied conditions. The apparent rate constants (k) were obtained from the slopes of the linear plots of $\ln(C_0/C_t)$ *versus* reaction time.

Increasing the reaction temperature led to a noticeable enhancement in the reaction rate, consistent with Arrhenius behavior. To determine the activation energy (E_a), the Arrhenius equation ($\ln k = \ln A - E_a/RT$) was applied. A linear plot of $\ln k$ *versus* $1/T$ (Fig. 10b) was obtained, and the slope ($-E_a/R$) was used to calculate the activation energy. The calculated E_a value was 55.70 kJ mol^{-1}. This moderate activation energy indicates that the BSB catalyst effectively lowers the energy barrier of the transesterification reaction, facilitating GyC formation. The obtained value confirms the good catalytic efficiency of BSB and supports the proposed surface-controlled reaction mechanism.

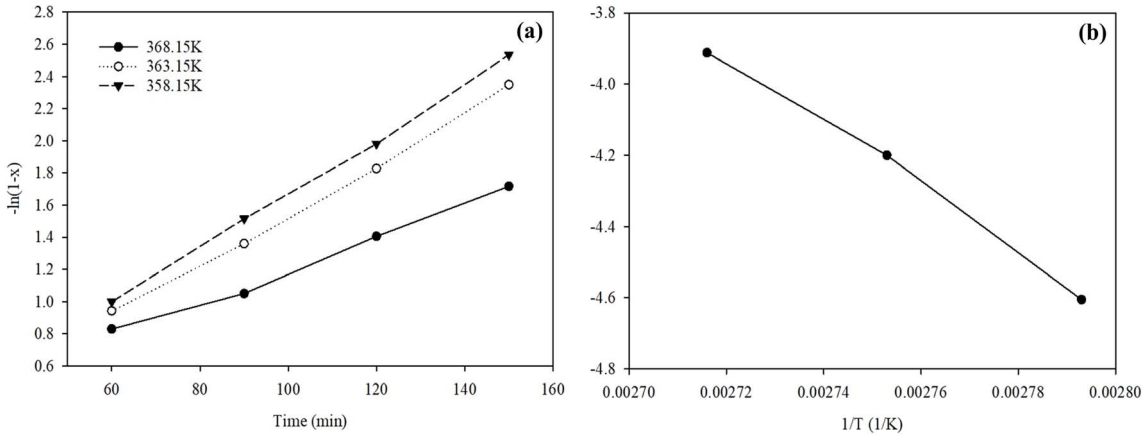

Fig. 10 Kinetic analysis of GyC synthesis using biochar catalysts. (a) Reaction time *versus* −ln(1 − *x*) and (b) Arrhenius plot of ln(*k*) *versus* 1/*T*.

3.6 Process simulations

The implemented process for GyC synthesis involves an integration of reaction and separation, optimized for product enrichment and recovery (Fig. 11). The enriched glycerol and DMC are preheated through a heat exchanger (HX-01) before they enter a continuous stirred-tank reactor (R-01). This reactor functions at 90.2 °C under ambient pressure. The transesterification reaction yields GyC, MeOH, and unreacted DMC as the main products. The separation occurs within a 25-stage distillation column (C-01) – the feed enters at stage 12 – operated at 0.185 bar. The DMC and MeOH as the distillate are isolated with a mole recovery rate of 0.9999, while GyC and water are recovered at the bottom with a mole recovery rate of 0.99997. Because of the azeotropic nature between DMC and MeOH,[61] extractive distillation columns (C-03 and C-04) give further enrichment. Column C-03 has 38 stages and functions at atmospheric pressure with aniline as the entrainer.[29] The aniline goes in at stage 4 and is maintained at a molar ratio of 1.2 to the feed at stage 34. The DMC and aniline are obtained at the bottom, while MeOH is the distillate, with recovery rates of 0.9999. Column C-04 is comprised of 11 stages, receiving feed at stage 5 and operating at 0.75 bar. The DMC and aniline mix are recovered with fresh make-up streams for continued runs. Final GyC enrichment happens in distillation column (D-02), attaining almost pure GyC (99.9%). After that, the enriched GyC and unreacted glycerol cool to 30 °C and go to storage tanks.

The process simulation found efficient separations within each column, which limited the loss of reactants and products. Table 7 lists the mass flow rates for three different feed capacities (1500, 3000, and 4500 kg h^{-1}). For instance, the mass flow rate of GyC was 1768.60 kg h^{-1} for a feed capacity of 1500 kg h^{-1}, which surpasses industry standards (99.9%). The use of biochar-based

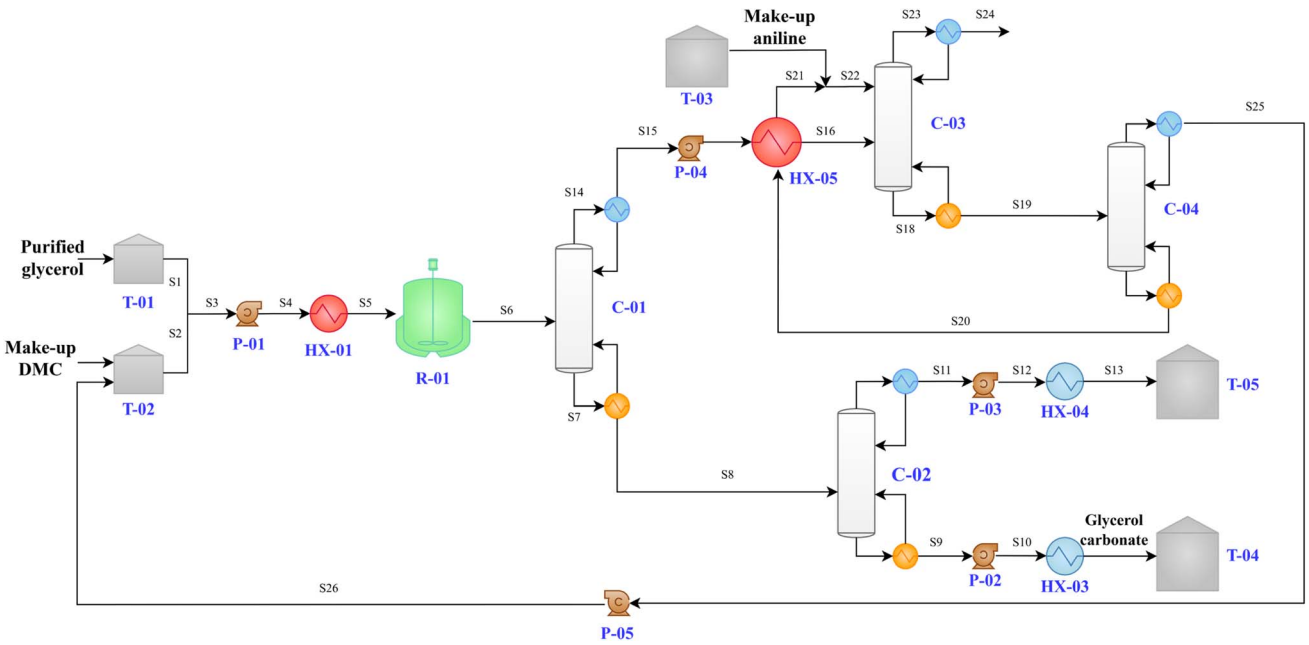

Fig. 11 Process flow diagram for GyC production *via* transesterification using biochar-based green catalysts.

Table 7 Results of the main mass flow analysis for GyC production *via* transesterification

Glycerol			DMC (S2)					DMC make up stream		Aniline (S22)			Aniline make up stream			GyC	
Feed capacity (kg h^{-1})	Mass fraction		Mass flow rate (kg h^{-1})	Mass fraction				Mass flow rate (kg h^{-1})	Mass fraction	Mass flow rate (kg h^{-1})	Mass fraction		Mass flow rate (kg h^{-1})	Mass fraction		Mass flow rate (kg h^{-1})	Mass fraction	
	GLY	H_2O		DMC	ANI	MEOH	H_2O		DMC	H_2O		ANI	DMC		Aniline	H_2O		GyC	Glycerol
1500	0.995	0.005	5223.79	0.99956	0.00016	0.00002	0.00026	1351.66	0.999	0.001	8151.86	0.99995	0.00005	0.83	0.999	0.001	1768.60	0.999	0.001
3000	0.995	0.005	10 447.59	0.99956	0.00016	0.00002	0.00026	2703.33	0.999	0.001	16 303.71	0.99995	0.00005	1.65	0.999	0.001	3537.21	0.999	0.001
4500	0.995	0.005	15 671.38	0.99956	0.00016	0.00002	0.00026	4054.99	0.999	0.001	24 455.57	0.99995	0.00005	2.48	0.999	0.001	5305.81	0.999	0.001

green catalysts in the transesterification reactor raises its sustainability by lowering impact and costs.[62] Additionally, using extractive distillation with aniline effectively beats azeotropic problems between DMC and MeOH.[63] This approach not only ensures high enrichment levels but also supports circular resource utilization by entrainer and reactant recycling.

3.7 Feasibility study (TEA)

3.7.1 OPEX analysis. The OPEX for GyC synthesis at feed rates of 1500, 3000, and 4500 kg h^{-1} displayed a huge effect from raw material charges, being approximately 70.00%, 72.49% and 72.99% of the total OPEX, respectively (Fig. 12).

Fig. 12 OPEX analysis for GyC production at feed capacities of (a) 1500 kg h^{-1}, (b) 3000 kg h^{-1}, and (c) 4500 kg h^{-1}.

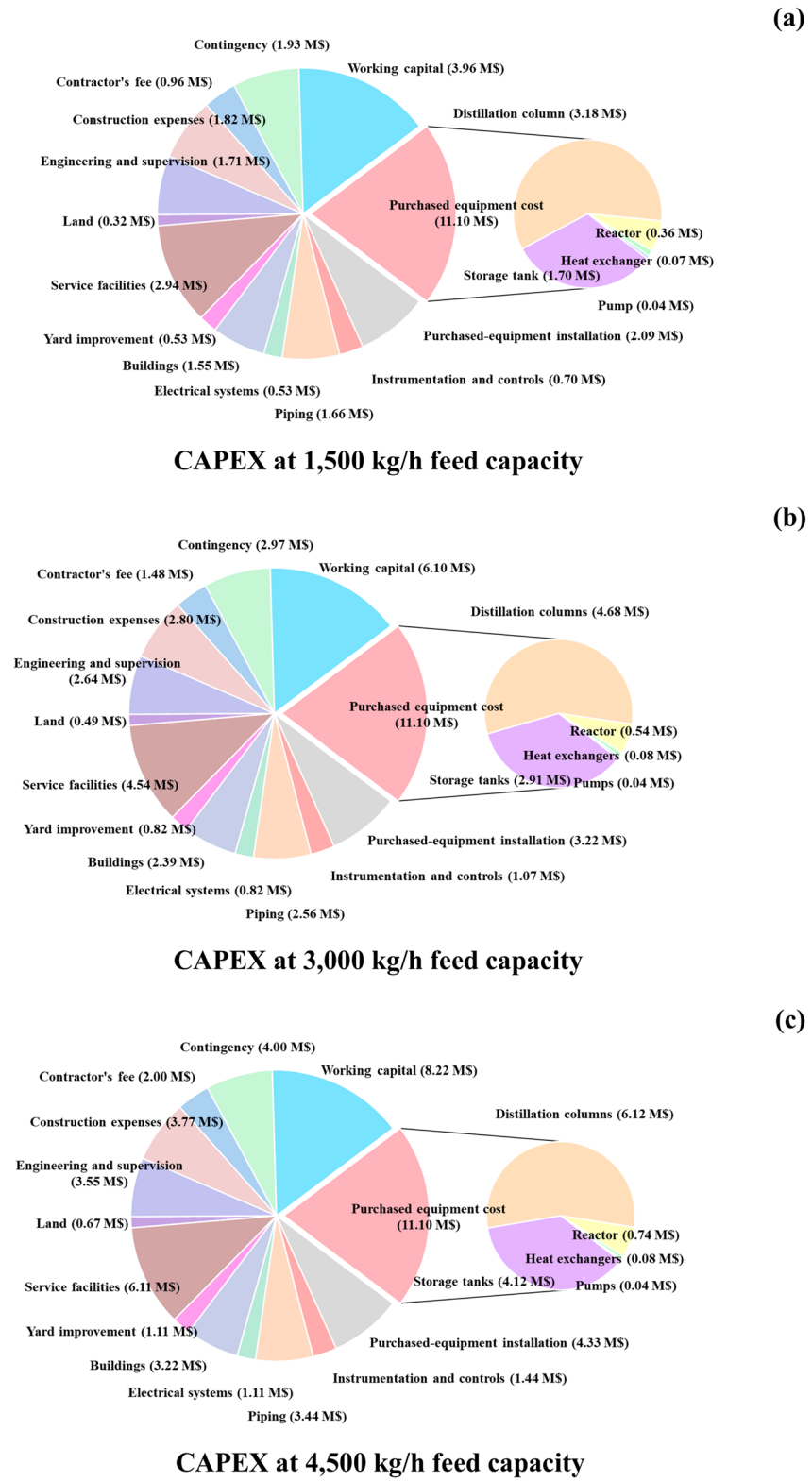

Fig. 13 CAPEX analysis for GyC production at feed capacities of (a) 1500 kg h^{-1}, (b) 3000 kg h^{-1}, and (c) 4500 kg h^{-1}.

This trend underscores the material-intensive nature of the process and emphasizes the critical need for optimizing raw material efficiency or sourcing cost-effective alternatives to improve the economic performance.[64] Utilities represent the second-largest cost component, contributing 11.58%, 10.57%, and 10.63% of OPEX as the capacity scaled up from 1500 kg h^{-1} to 3000 and 4500 kg h^{-1}, respectively, reflecting the higher energy needs at a larger scale.

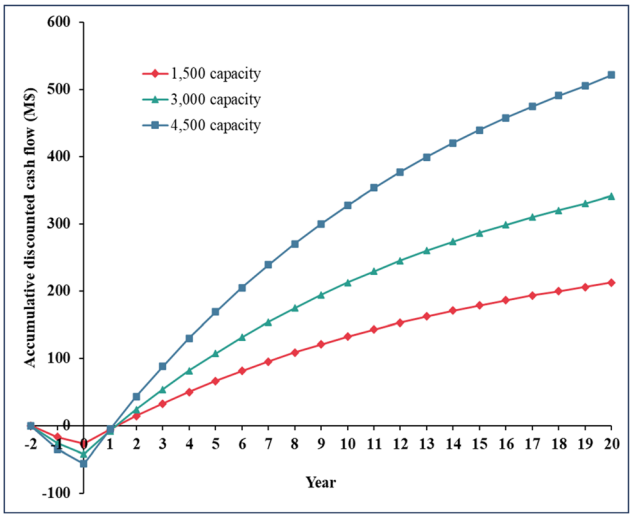

Fig. 14 Accumulative discounted cash flow analysis for GyC production at feed capacities of 1500 kg h^{-1}, 3000 kg h^{-1}, and 4500 kg h^{-1}.

Interestingly, labor costs remain constant in absolute terms at $0.39 million annually across all three capacities, but show significant economies of scale, decreasing from 1.39% of OPEX at 1500 kg h^{-1} to just 0.48% at 4500 kg h^{-1}. This efficiency highlights the benefits of fixed staffing levels in larger-scale operations. Other cost components, such as maintenance and repairs (2% of the FCI) and plant-overhead costs (5% of the TPC), scale predictably with capacity but contribute minimally to the overall OPEX. These findings align with existing research on process intensification and suggest that further improvements in raw material utilization and energy efficiency could significantly enhance profitability in large-scale GyC production.

3.7.2 CAPEX analysis. The CAPEX analysis for processing plants shows how costs spread out as well as how scaling affects key components (Fig. 13). Purchased equipment is the biggest cost, accounting for about 21% of total expenses for all capacities. Distillation columns and storage tanks are the most significant subcomponents.[64] As capacity increases, costs for service facilities, piping, and buildings also grow substantially, reflecting the infrastructural demands of larger-scale operations. Notably, working capital scales linearly with total investment, emphasizing its importance in ensuring operational readiness.

Interestingly, while economies of scale are evident in certain areas, such as land acquisition and contractor fees, the overall CAPEX exhibits a near-linear growth pattern. This suggests that while larger capacities benefit from some efficiencies, critical cost drivers like equipment and service facilities remain proportionally significant.

3.7.3 Accumulative discounted cash flow. Financial performance metrics further validate the economic advantages of scaling up GyC production (Fig. 14).[65] Over a 20 year horizon, the largest plant size (4500 kg h^{-1}) has a roughly 145% improved total discounted cash flow *versus* the smallest (1500 kg h^{-1}), while the mid-size plant (3000 kg h^{-1}) has a 60% gain over the smallest. The breakeven point is reached earlier in larger plants 2 years for the largest capacity *versus* 3 years for the smallest, highlighting the accelerated investment recovery.

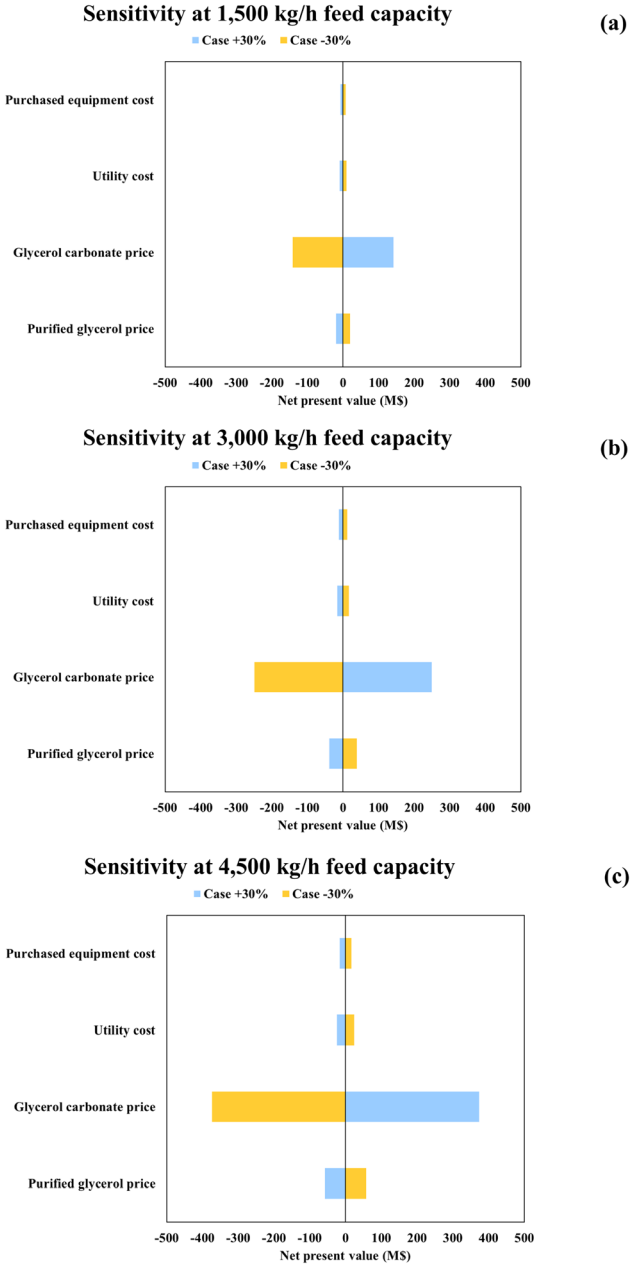

Fig. 15 Sensitivity analysis of key factors influencing the NPV of GyC production at feed capacities of (a) 1500 kg h^{-1}, (b) 3000 kg h^{-1}, and (c) 4500 kg h^{-1}.

The average yearly total discounted cash flow growth is much better for bigger plants (27% at 4500 kg h^{-1} compared to 18% at 1500 kg h^{-1}), which shows boosted financial performance over time. However, these benefits must be weighed against the nearly doubled initial CAPEX required for the largest facility compared to the smallest.

3.7.4 Sensitivity analysis. The sensitivity analysis, made at various feed capacities, demonstrates how essential cost

Table 8 Economic evaluation summary of GyC production at varying feed capacities

	Values		
Economic indicator	1500 kg h^{-1}	3000 kg h^{-1}	4500 kg h^{-1}
CAPEX ($)	26 042 024	40 155 738	54 069 839
OPEX ($ per year)	55 562 449	98 051 381	147 077 071
NPV ($)	212 651 091	341 154 464	521 781 052
PBP (year)	1.30	1.25	1.11
IRR (%)	83.85%	86.83%	97.28%

variables affect the NPV (Fig. 15). Across all capacities, the GyC price is the most important factor,[65] with significant variations in NPV observed for ± 30% changes in price. With an increased feed capacity, the magnitude of sensitivity rises as well. This highlights the need for efficient management of the GyC market price. The enriched glycerol price is the second most important, but utility and purchased equipment costs have a smaller impact on the NPV.

At higher feed capacities, sensitivity to the GyC price is increasingly pronounced, reflecting its critical role in profitability. Conversely, utility and equipment costs maintain a relatively stable influence across all scenarios. This analysis underscores the need for strategic pricing and cost optimization to ensure economic feasibility at different production scales.

3.7.5 Economic performance indicators. The economic evaluation of GyC production at the different feed capacities demonstrates significant advantages of scaling up operations (Table 8). While both the CAPEX and OPEX increase with capacity, the financial metrics indicate improved profitability at larger scales. The NPV rises dramatically from $212.65 million at 1500 kg h^{-1} to $521.78 million at 4500 kg h^{-1}, reflecting an enhanced economic viability. Concurrently, the PBP shortens from 1.30 years to just 1.11 years, indicating faster recovery of investment. Additionally, the IRR improves substantially from 83.85% to 97.28%, underscoring the higher attractiveness of larger-scale production. These findings highlight that increasing production capacity not only optimizes economic efficiency but also strengthens the feasibility and profitability of GyC production on an industrial scale.

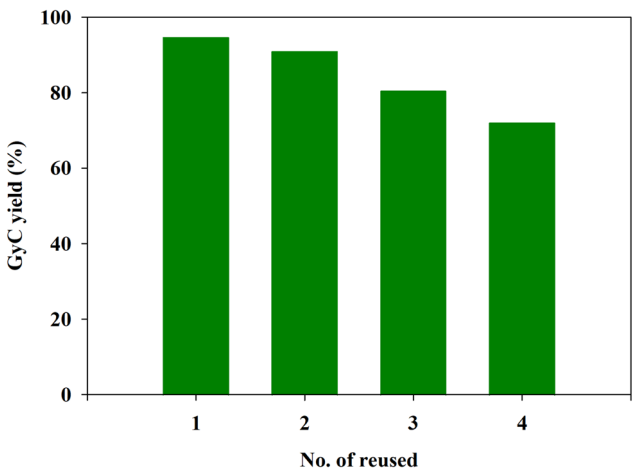

Fig. 16 Reusability study of banana bunch stalk biochar catalyst for GyC synthesis under optimized conditions.

3.8 Reusability of the catalyst

The BSB catalyst demonstrated a progressive loss of catalytic efficiency over four consecutive reaction cycles, with the obtained GyC yield declining to 72.04% by the fourth reuse (Fig. 16). This decline in activity is primarily attributed to potassium leaching, which resulted in a reduction of active basic sites. Elemental analysis revealed that the potassium content decreased by approximately 50% after four cycles (Fig. 5e and f), directly correlating with the observed decrease in catalytic performance. Concurrently, pH measurements showed a consistent downward trend (Fig. 6), aligning with a 46% reduction in total basicity from 3.66 mmol g^{-1} (fresh catalyst) to 2.00 mmol g^{-1} after four cycles, as determined by Hammett indicator titration. Although the reused catalyst retained moderate basic strength ($7.2 \leq H_- \leq 9.8$), the significant decrease in basic site density limited the availability of active sites required for efficient transesterification. These results emphasize the importance of maintaining both surface alkalinity and structural integrity for sustained catalytic performance.

The FT-IR analysis further confirmed chemical changes on the fourth-cycle catalyst, consistent with its reduced activity (Fig. 3). A noticeable decrease in the intensity of the band at 1642.4 cm^{-1}, associated with carbonate species such as K_2CO_3,[47] was observed, indicating partial depletion of potassium-containing phases due to leaching during repeated reactions. The characteristic K_2CO_3 band at 1400.3 cm^{-1} in the fresh catalyst shifted to 1418.2 cm^{-1} and 1477.8 cm^{-1} in the reused catalyst,[46] accompanied by reduced intensity, suggesting structural alteration or partial degradation of the carbonate phase within the catalyst matrix. These structural modifications correlate well with the decline in GyC yield, confirming that potassium leaching and carbonate phase instability are major contributors to catalyst deactivation. The absorption peaks at 1042.8 and 1079.8 cm^{-1} were assigned to C–O stretching vibrations of oxygenated functional groups,[45] indicating possible surface restructuring during repeated use.

4. Conclusions

This study successfully demonstrated the synthesis of GyC *via* transesterification using a self-activated potassium-rich mesoporous biochar catalyst derived from BS agricultural waste. Unlike conventional alkali-impregnated catalysts, the developed biochar contained intrinsic basic active sites without external chemical modification, enhancing its sustainability and cost-effectiveness. By employing RSM-CCD, the research optimized critical process parameters, achieving a maximum GyC yield of 92.40% under optimal conditions.

The biochar catalyst exhibited strong basicity and high catalytic efficiency, attributed to its potassium-enriched composition and mesoporous structure. A clear structure–

activity relationship was established between intrinsic mineral species and catalytic performance, confirming that naturally occurring potassium compounds act as effective active sites for transesterification. Kinetic studies indicated that the reaction follows a pseudo-first-order mechanism with an E_a of 55.70 kJ mol^{-1}, verifying that the process operates under a chemically controlled regime rather than mass transfer limitation.

Although catalyst deactivation occurred over multiple cycles due to potassium leaching, this finding provides important insight into stability challenges of mineral-rich biochar catalysts and offers direction for future structural stabilization strategies.

Process simulation verified the reaction could be scaled up and that it achieved a high product enrichment to near purity (99.9%) with effective resource utilization. Importantly, this work integrates catalyst design, reaction optimization, kinetic validation, process simulation, and TEA within a unified framework an approach rarely reported for GyC production. The TEA revealed that production becomes more profitable when scaled up. Larger production sizes shortened the PBP and increased the NPV and IRR. This study demonstrates a scalable waste-to-value catalytic platform that advances circular bioeconomy strategies, reduces reliance on chemically modified catalysts, and supports sustainable industrial glycerol upgrading.

Conflicts of interest

The authors declare that there are no conflicts of interest.

Data availability

Data are available within the article.

Acknowledgements

The authors sincerely acknowledge Ms Bantita Poolsawat and Ms Ananya Tudnainhu, students at Rajamangala University of Technology Srivijaya, for their dedicated assistance and meaningful contributions to this study. This research was supported by National Science, Research and Innovation Fund (NSRF) and Rajamangala University of Technology Srivijaya (ref. 215090).

References

1 W. K. Teng, G. C. Ngoh, R. Yusoff and M. K. Aroua, *Energy Convers. Manage.*, 2014, **88**, 484–497.
2 Y. Liu, B. Zhong and A. Lawal, *RSC Adv.*, 2022, **12**, 27997–28008.
3 N. Nirmala, J. Arun, S. Palanisamy, R. S. E. Ravindran, M. Abbas, S. Kalathil and M. Z. Rahman, *RSC Adv.*, 2025, **15**, 42513–42521.
4 G. Pradhan and Y. C. Sharma, *J. Clean. Prod.*, 2021, **315**, 127860.
5 A. Sarkar, T. Tyagi, S. Sharma, V. Joshi, P. Gogoi, A. Puzari and B. Paul, *Catal. Today*, 2025, **448**, 115164.
6 Z. Cao, G. Wu, X. Wang, L. Deng, J. Wan, Y. Liu, J. Kan, C. Shang and Z. Guo, *Mol. Catal.*, 2024, **564**, 114348.
7 X. Chen, X. Shu, Y. Zhu, J. Zhang, Z. Chai, H. Song, Z. An and J. He, *Chin. J. Chem. Eng.*, 2024, **72**, 153–163.
8 M. H. Ab. Rahim, N. A. S. Zuhaimi, A. S. Saud, V. R. Madduluri, H. Alshammari and G. P. Maniam, *Fuel*, 2024, **357**, 129774.
9 G. P. Fernandes and G. D. Yadav, *Catal. Today*, 2018, **309**, 153–160.
10 G. M. de Paula, J. G. Eid, L. D. N. R. de Paula and D. Cardoso, *Catal. Today*, 2024, **442**, 114953.
11 J. Kowalska-Kuś, A. Held, K. Nowińska and K. Góra-Marek, *Fuel*, 2024, **362**, 130757.
12 J. Jitjamnong, P. Khongprom, T. Ratanawilai and S. Ratanawilai, *RSC Adv.*, 2024, **14**, 5941–5958.
13 H. Tang, C. Luo, H. Lu, K. Wu, Y. Liu, Y. Zhu, B. Wang and B. Liang, *Chem. Eng. J.*, 2024, **481**, 148552.
14 S. Sahani, S. N. Upadhyay and Y. C. Sharma, *Ind. Eng. Chem. Res.*, 2021, **60**, 67–88.
15 J. Esteban, E. Fuente, A. Blanco, M. Ladero and F. Garcia-Ochoa, *Chem. Eng. J.*, 2015, **260**, 434–443.
16 A. Chotchuang, P. Kunsuk, A. Phanpitakkul, S. Chanklang, M. Chareonpanich and A. Seubsai, *Catal. Today*, 2022, **388–389**, 351–359.
17 G. Pradhan and Y. C. Sharma, *Fuel*, 2021, **284**, 118966.
18 P. U. Okoye, S. Wang, W. A. Khanday, S. Li, T. Tang and L. Zhang, *Renew. Energy*, 2020, **146**, 2676–2687.
19 S. Wang, J. Wang, P. Sun, L. Xu, P. U. Okoye, S. Li, L. Zhang, A. Guo, J. Zhang and A. Zhang, *J. Clean. Prod.*, 2019, **211**, 330–341.
20 Q. Fan, J. Sun, L. Chu, L. Cui, G. Quan, J. Yan, Q. Hussain and M. Iqbal, *Chemosphere*, 2018, **207**, 33–40.
21 H. Örtün, M. Sert and E. Sert, *Biomass Bioenergy*, 2025, **194**, 107624.
22 K. Shikhaliyev, P. U. Okoye and B. H. Hameed, *Energy Convers. Manage.*, 2018, **165**, 794–800.
23 A. Das, D. Shi, G. Halder and S. L. Rokhum, *Fuel*, 2022, **330**, 125511.
24 B. Changmai, I. B. Laskar and S. L. Rokhum, *J. Taiwan Inst. Chem. Eng.*, 2019, **102**, 276–282.
25 P. Saetiao, N. Kongrit, P. Solod, S. B. Sufian and J. Jitjamnong, *ACS Omega*, 2025, **10**, 44398–44414.
26 J. Jitjamnong, C. Thunyaratchatanon, A. Luengnaruemitchai, N. Kongrit, N. Kasetsomboon, A. Sopajarn, N. Chuaykarn and N. Khantikulanon, *Biomass Convers. Biorefinery*, 2021, **11**, 2795–2811.
27 B. Chalermthai, C. Sriharuethai, B. D. Olsen, K. Ngaosuwan, A. Soottitantawat, S. Assabumrungrat and P. Charoensuppanimit, *Sci. Rep.*, 2025, **15**, 1753.
28 T. Attarbachi, M. Kingsley and V. Spallina, *Ind. Eng. Chem. Res.*, 2024, **63**, 4905–4917.
29 B. Y. Yu, *J. Taiwan Inst. Chem. Eng.*, 2020, **117**, 19–25.
30 M. S. Peters, K. D. Timmerhaus and R. E. West, *Plant Design and Economics for Chemical Engineers*, McGraw-Hill, New York, 5th edn, 2003.
31 S. Luanwuthi, P. Iamprasertkun, T. Akkharaamnuay, C. Kunyawut, A. Phukhrongthung and C. Puchongkawarin, *ACS Sustainable Chem. Eng.*, 2024, **12**, 14446–14458.

32 D. C. Makepa, C. H. Chihobo and D. Musademba, *Heliyon*, 2023, **9**, e22261.
33 S. Jenkins, 2024 CEPCI Updates, 2024, https://www.chemengonline.com/2024-cepci-updates-june-prelim-and-may-final/, accessed on 2025-12-01.
34 T. Attarbachi, M. D. Kingsley and V. Spallina, *Fuel*, 2023, **340**, 127485.
35 S. Bugosen, I. D. Mantilla and F. Tarazona-Vasquez, *Heliyon*, 2020, **6**, e05778.
36 V. Varalakksmi, R. Hariharan, S. Rahul, S. Prabakaran and A. Arumugam, *Ind. Crop. Prod.*, 2025, **223**, 120049.
37 J. Jitjamnong, P. Khongprom, T. Ratanawilai and S. Ratanawilai, *Case Stud. Chem. Environ. Eng.*, 2023, **8**, 100465.
38 B. Y. Yu, P. J. Wu, C. C. Tsai and S. T. Lin, *J. CO2 Util.*, 2020, **41**, 101254.
39 R. Turton, J. A. Shaeiwitz, D. Bhattacharyya and W. B. Whiting, *Analysis, Synthesis, and Design of Chemical Processes*, Prentice Hall, Boston, 5th edn, 2018.
40 R. Junsittiwate, T. R. Srinophakun and S. Sukpancharoen, *Energy Sustain. Dev.*, 2022, **66**, 140–150.
41 K. Saikia, N. S. Moyon, R. Piloto-Rodríguez, F. Chai, S. Basumatary and S. L. Rokhum, *Sustain. Chem. Pharm.*, 2023, **36**, 101271.
42 G. Pathak, D. Das, K. Rajkumari and S. L. Rokhum, *Green Chem.*, 2018, **20**, 2365–2373.
43 A. K. Rajak, M. Harikrishna, D. L. Mahato, U. Anandamma, R. Pothu, P. K. Sarangi, U. K. Sahoo, V. Vennu, R. Boddula and M. S. L. Karuna, *J. Taiwan Inst. Chem. Eng.*, 2025, **177**, 105804.
44 Y. Mao, Y. Jiang, X. Shao, X. Lv, J. Ma and S. Cen, *Process Saf. Environ. Prot.*, 2024, **191**, 1617–1632.
45 M. Gohain, A. Devi and D. Deka, *Ind. Crops Prod.*, 2017, **109**, 8–18.
46 S. F. Basumatary, B. Das, S. Brahma and S. Basumatary, *Bioresour. Technol. Rep.*, 2025, **29**, 102018.
47 S. Brahma, B. Basumatary, S. F. Basumatary, B. Das, S. Brahma, S. L. Rokhum and S. Basumatary, *Fuel*, 2023, **336**, 127150.
48 Z. Mansoorsamaei, D. Mowla, F. Esmaeilzadeh and K. Dashtian, *Fuel*, 2024, **357**, 129821.
49 B. Nath, B. Basumatary, S. Brahma, B. Das, P. Kalita, S. L. Rokhum and S. Basumatary, *Energy*, 2023, **270**, 126976.
50 C. B. Ezekannagha, O. D. Onukwuli, J. I. Obibuenyi and D. I. Udunwa, *Chem. Eng. Res. Des.*, 2023, **200**, 256–265.
51 I. M. Mendonça, O. A. R. L. Paes, P. J. S. Maia, M. P. Souza, R. A. Almeida, C. C. Silva, S. Duvoisin and F. A. de Freitas, *Renew. Energy*, 2019, **130**, 103–110.
52 B. Saelim, T. Ratanawilai and S. Ratanawilai, *ACS Omega*, 2023, **8**, 48904–48914.
53 Z. Liu, B. Li, F. Qiao, Y. Zhang, X. Wang, Z. Niu, J. Wang, H. Lu, S. Su, R. Pan, Y. Wang and Y. Xue, *ACS Omega*, 2022, **7**, 5032–5038.
54 B. Olaniyan and B. Saha, *Energies*, 2020, **13**, 741.
55 N. Kamairudin, S. S. Hoong, L. C. Abdullah, H. Ariffin and D. R. A. Biak, *Molecules*, 2021, **26**, 648.
56 L. Y. Lai, P. C. Lau, T. L. Kwong and K. F. Yung, *J. Organomet. Chem.*, 2025, **1025**, 123467.
57 I. Kandola, T. Kivevele, A. Hilonga, B. Kichonge, P. Maina, R. C. Ramkat, O. Castro-Ocampo, C. Delesma, J. Muñiz and P. U. Okoye, *J. Environ. Chem. Eng.*, 2025, **13**, 116030.
58 Y. Li, H. Zhao, W. Xue, F. Li and Z. Wang, *Nanomaterials*, 2022, **12**, 1972.
59 D. S. Argüello, I. Barroso-Martín, N. F. Bálsamo, E. Rodríguez-Castellón, G. A. Eimer and M. E. Crivello, *Chem. Eng. Res. Des.*, 2024, **212**, 555–568.
60 C. Wu, Z. Wang, Z. Wei, D. Li, Z. Yin, Q. Wu, S. Chen, Y. Gan, M. Lian and Z. Wang, *J. Environ. Chem. Eng.*, 2024, **12**, 113720.
61 K. Y. Hsu, Y. C. Hsiao and I. L. Chien, *Ind. Eng. Chem. Res.*, 2010, **49**, 735–749.
62 A. R. P. Gonçalves, A. P. C. Ribeiro, S. Orišková, L. M. D. R. S. Martins, A. F. Cristino and R. G. dos Santos, *Molecules*, 2022, **27**, 5634.
63 I. Rodriguez-Donis, N. Shcherbakova, E. Parascandolo, J. Abildskov and V. Gerbaud, *Chem. Eng. Res. Des.*, 2024, **205**, 443–458.
64 O. Del-Mazo-Alvarado, C. Prieto, A. Sánchez, C. Ramírez-Márquez, A. Bonilla-Petriciolet and M. Martín, *ChemSusChem*, 2024, **17**, e202301546.
65 K. Pandit, C. Jeffrey, J. Keogh, M. S. Tiwari, N. Artioli and H. G. Manyar, *Ind. Eng. Chem. Res.*, 2023, **62**, 9201–9210.